TVD Flux Vector Splitting Algorithms Applied to the Solution of the Euler and Navier-Stokes Equations in Three-Dimensions – Part I

EDISSON SÁVIO DE GÓES MACIEL
IEA- Aeronautical Engineering Division
ITA – Aeronautical Technological Institute
Praça Mal. Eduardo Gomes, 50 – Vila das Acácias – São José dos Campos – SP – 12228-900
BRAZIL
edissonsavio@yahoo.com.br

Abstract: - In the present work, the Steger and Warming, the Van Leer, the Liou and Steffen Jr. and the Radespiel and Kroll schemes are implemented, on a finite volume context and using a structured spatial discretization, to solve the Euler and the Navier-Stokes equations in three-dimensions. A MUSCL ("Monotone Upstream-centered Schemes for Conservation Laws") approach is implemented in these schemes aiming to obtain second order spatial accuracy and TVD ("Total Variation Diminishing") high resolution properties. An implicit formulation is employed to the Euler equations, whereas the Navier-Stokes equations use an explicit formulation. The algebraic turbulence models of Cebeci and Smith and of Baldwin and Lomax are implemented. The problems of the supersonic flow along a compression corner (inviscid case), and of the supersonic flow along a ramp (viscous case) are solved. The results have demonstrated that the most severe and most accurate results are obtained with the Liou and Steffen Jr. TVD scheme. The turbulent results are presented in the second part of this work.

Key-Words: - Steger and Warming algorithm, Van Leer algorithm, Liou and Steffen Jr. algorithm, Radespiel and Kroll algorithm, TVD high resolution schemes, Turbulence models, Euler and Navier-Stokes equations, Three-Dimensions.

1 Introduction

Conventional non-upwind algorithms have been used extensively to solve a wide variety of problems ([1-2]). Conventional algorithms are somewhat unreliable in the sense that for every different problem (and sometimes, every different case in the same class of problems) artificial dissipation terms must be specially tuned and judicially chosen for convergence. Also, complex problems with shocks and steep compression and expansion gradients may defy solution altogether.

Upwind schemes are in general more robust but are also more involved in their derivation and application. Some upwind schemes that have been applied to the Euler equations are: [3-7]. Some comments about these methods are reported below:

[3] presented a work that emphasized that several numerical schemes to the solution of the hyperbolic conservation equations were based on exploring the information obtained in the solution of a sequence of Riemann problems. It was verified that in the existent schemes the major part of these information was degraded and that only certain solution aspects were solved. It was demonstrated that the information could be preserved by the construction of a matrix with a certain "U property". After the construction of this matrix, its eigenvalues could be considered as wave velocities of the Riemann problem and the U_L-U_R projections over the matrix's eigenvectors would be the jumps which occur between intermediate stages.

[4] developed a method that used the remarkable property that the nonlinear flux vectors of the inviscid gasdynamic equations in conservation law form were homogeneous functions of degree one of the vector of conserved variables. This property readily permitted the splitting of the flux vectors into sub-vectors by similarity transformations so that each sub-vector had associated with it a specified eigenvalue spectrum. As a consequence of flux vector splitting, new explicit and implicit dissipative finite-difference schemes were developed for first-order hyperbolic systems of equations.

[5] suggested an upwind scheme based on the flux vector splitting concept. This scheme considered the fact that the convective flux vector components could be written as flow Mach number polynomial functions, as main characteristic. Such polynomials presented the particularity of having the minor possible degree and the scheme had to satisfy seven basic properties to form such polynomials. This scheme was presented to the

Euler equations in Cartesian coordinates and three-dimensions.

[6] proposed a new flux vector splitting scheme. They declared that their scheme was simple and its accuracy was equivalent and, in some cases, better than the [3] scheme accuracy in the solutions of the Euler and the Navier-Stokes equations. The scheme was robust and converged solutions were obtained so fast as the [3] scheme. The authors proposed the approximated definition of an advection Mach number at the cell face, using its neighbor cell values via associated characteristic velocities. This interface Mach number was so used to determine the upwind extrapolation of the convective quantities.

[7] emphasized that the [6] scheme had its merits of low computational complexity and low numerical diffusion as compared to other methods. They also mentioned that the original method had several deficiencies. The method yielded local pressure oscillations in the shock wave proximities, adverse mesh and flow alignment problems. In [7], a hybrid flux vector splitting scheme, which alternated between the [6] scheme and the [5] scheme, in the shock wave regions, is proposed, assuring that resolution of strength shocks was clear and sharply defined.

Second order spatial accuracy can be achieved by introducing more upwind points or cells in the schemes. It has been noted that the projection stage, whereby the solution is projected in each cell face (i-½,i+½) on piecewise constant states, is the cause of the first order space accuracy of the Godunov schemes ([8]). Hence, it is sufficient to modify the first projection stage without modifying the Riemann solver, in order to generate higher spatial approximations. The state variables at the interfaces are thereby obtained from an extrapolation between neighboring cell averages. This method for the generation of second order upwind schemes based on variable extrapolation is often referred to in the literature as the MUSCL ("Monotone Upstream-centered Schemes for Conservation Laws") approach. The use of nonlinear limiters in such procedure, with the intention of restricting the amplitude of the gradients appearing in the solution, avoiding thus the formation of new extrema, allows that first order upwind schemes be transformed in TVD high resolution schemes with the appropriate definition of such nonlinear limiters, assuring monotone preserving and total variation diminishing methods.

Traditionally, implicit numerical methods have been praised for their improved stability and condemned for their large arithmetic operation counts ([9]). On the one hand, the slow convergence rate of explicit methods become they so unattractive to the solution of steady state problems due to the large number of iterations required to convergence, in spite of the reduced number of operation counts per time step in comparison with their implicit counterparts. Such problem is resulting from the limited stability region which such methods are subjected (the Courant condition). On the other hand, implicit schemes guarantee a larger stability region, which allows the use of CFL numbers above 1.0, and fast convergence to steady state conditions. Undoubtedly, the most significant efficiency achievement for multidimensional implicit methods was the introduction of the Alternating Direction Implicit (ADI) algorithms by [10-12], and fractional step algorithms by [13]. ADI approximate factorization methods consist in approximating the Left Hand Side (LHS) of the numerical scheme by the product of one-dimensional parcels, each one associated with a different spatial coordinate direction, which retract nearly the original implicit operator. These methods have been largely applied in the CFD community and, despite the fact of the error of the approximate factorization, it allows the use of large time steps, which results in significant gains in terms of convergence rate in relation to explicit methods.

There is a practical necessity in the aeronautical industry and in other fields of the capability of calculating separated turbulent compressible flows. With the available numerical methods, researches seem able to analyze several separated flows, three-dimensional in general, if an appropriated turbulence model is employed. Simple methods as the algebraic turbulence models of [14-15] supply satisfactory results with low computational cost and allow that the main features of the turbulent flow be detected.

[16] performed a comparison between the [17] and [18] schemes implemented coupled with the [14-15] models to accomplish turbulent flow simulations in three-dimensions. The Navier-Stokes equations in conservative and integral forms were solved, employing a finite volume formulation and a structured spatial discretization. The [17] scheme is a predictor/corrector method which performs coupled time and space discretizations, whereas the [18] algorithm is a symmetrical scheme and its time discretization is performed by a Runge-Kutta method. Both schemes are second order accurate in space and time and require artificial dissipation to guarantee stability. The steady state problem of the supersonic turbulent flow along a ramp was studied. The results have demonstrated that both turbulence models predicted appropriately the boundary layer

separation region formed at the compression corner, reducing, however, its extension in relation to the laminar solution, as expected.

In the present work, the [4-7] schemes are implemented, on a finite volume context and using a structured spatial discretization, to solve the Euler and the laminar/turbulent Navier-Stokes equations in the three-dimensional space. All schemes are flux vector splitting ones and in their original implementations are first order accurate. A MUSCL approach is implemented in these schemes aiming to obtain second order spatial accuracy. The Van Leer, the Van Albada and the Minmod nonlinear limiters are employed to guarantee such accuracy and TVD high resolution properties. These flux vector splitting schemes employ approximate factorizations in ADI form to solve implicitly the Euler equations. To solve the laminar/turbulent Navier-Stokes equations, an explicit formulation based on a dimensional splitting procedure is employed. All schemes are first order accurate in time in their implicit and explicit versions. Turbulence is taken into account considering two algebraic models, namely: [14-15]. The algorithms are accelerated to the steady state solution using a spatially variable time step, which has demonstrated effective gains in terms of convergence rate ([19-20]). All four schemes are applied to the solution of the physical problems of the supersonic flow along a compression corner, in the inviscid case, and of the supersonic flow along a ramp, in the laminar and turbulent cases. The results have demonstrated that the most severe and most accurate results are obtained with the [6] TVD high resolution scheme. The turbulent results are presented in the second part of this study (Part II).

The main contribution of this work to the CFD (Computational Fluid Dynamics) community is the extension of the TVD high resolution algorithms of [4-7] to the three-dimensional space, following a finite volume formulation, and their implementation coupled with two different algebraic turbulence models to simulate viscous turbulent flows, which characterizes an original contribution in the field of high resolution structured numerical algorithms. The implicit implementation in three-dimensions of these algorithms is also a meaningful contribution.

2 Navier-Stokes Equations

As the Euler equations can be obtained from the Navier-Stokes ones by disregarding the viscous vectors, only the formulation to the latter will be presented. The Navier-Stokes equations in integral conservative form, employing a finite volume formulation and using a structured spatial discretization, to three-dimensional simulations, can be written as:

$$\partial Q/\partial t + 1/V \int_V \vec{\nabla} \cdot \vec{P} dV = 0\,, \tag{1}$$

where V is the cell volume, which corresponds to an hexahedron in the three-dimensional space; Q is the vector of conserved variables; and $\vec{P} = (E_e - E_v)\vec{i} + (F_e - F_v)\vec{j} + (G_e - G_v)\vec{k}$ represents the complete flux vector in Cartesian coordinates, with the subscript "e" related to the inviscid contributions or the Euler contributions and "v" is related to the viscous contributions. These components of the complete flux vector, as well the vector of conserved variables, are described below:

$$Q = \begin{Bmatrix} \rho \\ \rho u \\ \rho v \\ \rho w \\ e \end{Bmatrix},\ E_e = \begin{Bmatrix} \rho u \\ \rho u^2 + p \\ \rho uv \\ \rho uw \\ (e+p)u \end{Bmatrix},\ F_e = \begin{Bmatrix} \rho v \\ \rho uv \\ \rho v^2 + p \\ \rho vw \\ (e+p)v \end{Bmatrix}; \tag{2}$$

$$G_e = \begin{Bmatrix} \rho w \\ \rho uw \\ \rho vw \\ \rho w^2 + p \\ (e+p)w \end{Bmatrix},\ E_v = \frac{1}{\mathrm{Re}} \begin{Bmatrix} 0 \\ \tau_{xx} \\ \tau_{xy} \\ \tau_{xz} \\ \tau_{xx}u + \tau_{xy}v + \tau_{xz}w - q_x \end{Bmatrix}; \tag{3}$$

$$F_v = \frac{1}{\mathrm{Re}} \begin{Bmatrix} 0 \\ \tau_{yx} \\ \tau_{yy} \\ \tau_{yz} \\ \tau_{yx}u + \tau_{yy}v + \tau_{yz}w - q_y \end{Bmatrix},\ G_v = \frac{1}{\mathrm{Re}} \begin{Bmatrix} 0 \\ \tau_{zx} \\ \tau_{zy} \\ \tau_{zz} \\ \tau_{zx}u + \tau_{zy}v + \tau_{zz}w - q_z \end{Bmatrix}. \tag{4}$$

In these equations, the components of the viscous stress tensor are defined as:

$$\tau_{xx} = 2(\mu_M + \mu_T)\partial u/\partial x - 2/3(\mu_M + \mu_T)(\partial u/\partial x + \partial v/\partial y + \partial w/\partial z); \tag{5}$$

$$\tau_{xy} = (\mu_M + \mu_T)(\partial u/\partial y + \partial v/\partial x)\,; \tag{6}$$

$$\tau_{xz} = (\mu_M + \mu_T)(\partial u/\partial z + \partial w/\partial x)\,; \tag{7}$$

$$\tau_{yy} = 2(\mu_M + \mu_T)\partial v/\partial y - 2/3(\mu_M + \mu_T)(\partial u/\partial x + \partial v/\partial y + \partial w/\partial z); \tag{8}$$

$$\tau_{yz} = (\mu_M + \mu_T)(\partial v/\partial z + \partial w/\partial y)\,; \tag{9}$$

$$\tau_{zz} = 2(\mu_M + \mu_T)\partial w/\partial z - 2/3(\mu_M + \mu_T)(\partial u/\partial x + \partial v/\partial y + \partial w/\partial z). \tag{10}$$

The components of the conductive heat flux vector are defined as follows:

$$q_x = -\gamma\left(\mu_M/\mathrm{Pr}d + \mu_T/\mathrm{Pr}d_T\right)\partial e_i/\partial x\,; \quad (11)$$

$$q_y = -\gamma\left(\mu_M/\mathrm{Pr}d + \mu_T/\mathrm{Pr}d_T\right)\partial e_i/\partial y\,; \quad (12)$$

$$q_z = -\gamma\left(\mu_M/\mathrm{Pr}d + \mu_T/\mathrm{Pr}d_T\right)\partial e_i/\partial z\,. \quad (13)$$

The quantities that appear above are described as follows: ρ is the fluid density, *u*, *v* and *w* are the Cartesian components of the flow velocity vector in the *x*, *y* and *z* directions, respectively; *e* is the total energy per unit volume of the fluid; *p* is the fluid static pressure; e_i is the fluid internal energy, defined as:

$$e_i = e/\rho - 0.5\left(u^2 + v^2 + w^2\right); \quad (14)$$

the τ's represent the components of the viscous stress tensor; Prd is the laminar Prandtl number, which assumed a value of 0.72 in the present simulations; $\mathrm{Prd_T}$ is the turbulent Prandtl number, which assumed a value of 0.9; the *q*'s represent the components of the conductive heat flux; μ_M is the fluid molecular viscosity; μ_T is the fluid turbulent viscosity; γ is the ratio of specific heats at constant pressure and volume, respectively, which assumed a value 1.4 to the atmospheric air; and Re is the Reynolds number of the viscous simulation, defined by:

$$\mathrm{Re} = \rho u_{REF} l/\mu_M\,, \quad (15)$$

where u_{REF} is a characteristic flow velocity and *l* is a configuration characteristic length. The molecular viscosity is estimated by the empiric Sutherland formula:

$$\mu_M = bT^{1/2}/(1+S/T), \quad (16)$$

where T is the absolute temperature (K), b = $1.458\text{x}10^{-6}$ Kg/(m.s.$\mathrm{K}^{1/2}$) and S = 110.4 K, to the atmospheric air in the standard atmospheric conditions ([21]).

The Navier-Stokes equations were dimensionless in relation to the freestream density, ρ_∞, the freestream speed of sound, a_∞, and the freestream molecular viscosity, μ_∞, for the compression corner and ramp problems. To allow the solution of the matrix system of five equations to five unknowns described by Eq. (1), it is employed the state equation of perfect gases, in its two versions, presented below:

$$p = (\gamma-1)\left[e - 0.5\rho(u^2+v^2+w^2)\right] \text{ or } p = \rho RT\,, \quad (17)$$

with *R* being the specific gas constant, which to atmospheric air assumes the value 287 J/(Kg.K). The total enthalpy is determined by:

$$H = (e+p)/\rho\,. \quad (18)$$

The geometrical characteristics of the present implementation, namely: cell definition, cell volume, flux areas and unit normal vectors to each flux area, are defined in [22-23].

3 [4] Algorithm

3.1 Theory for the One-Dimensional Case

If the homogeneous Euler equations are put in characteristic form

$$\partial W/\partial t + \Lambda\,\partial W/\partial x = 0\,, \quad (19)$$

where *W* is the vector of characteristic variables (defined in [8]) and Λ is the diagonal matrix of eigenvalues, the upwind scheme:

$$u_i^{n+1} - u_i^n = -\Delta t/\Delta x\left[\hat{a}^+\left(u_i^n - u_{i-1}^n\right) + \hat{a}^-\left(u_{i+1}^n - u_i^n\right)\right], \quad (20)$$

where *u* is a scalar property, $\hat{a}^+ = 0.5\left(\hat{a} + |\hat{a}|\right)$ and $\hat{a}^- = 0.5\left(\hat{a} - |\hat{a}|\right)$, can be applied to each of the three characteristic variables separately, with the definitions

$$\lambda_l^+ = 0.5\left(\lambda_l + |\lambda_l|\right) \quad \text{and} \quad \lambda_l^- = 0.5\left(\lambda_l - |\lambda_l|\right) \quad (21)$$

for each of the eigenvalues of Λ

$$\Lambda = \begin{bmatrix} \lambda_1 & & \\ & \lambda_2 & \\ & & \lambda_3 \end{bmatrix} = \begin{bmatrix} u & & \\ & u+a & \\ & & u-a \end{bmatrix}. \quad (22)$$

This defines two diagonal matrices $\Lambda^\pm$:

$$\Lambda^\pm = \begin{bmatrix} \lambda_1^\pm & & \\ & \lambda_2^\pm & \\ & & \lambda_3^\pm \end{bmatrix} = \begin{bmatrix} 0.5\left(u \pm |u|\right) & & \\ & 0.5\left(u+a \pm |u+a|\right) & \\ & & 0.5\left(u-a \pm |u-a|\right) \end{bmatrix}, \quad (23)$$

where Λ^+ has only positive eigenvalues, Λ^- only negative eigenvalues, and such that

$$\Lambda = \Lambda^+ + \Lambda^- \quad \text{and} \quad |\Lambda| = \Lambda^+ - \Lambda^-; \tag{24}$$

$$\text{or} \quad \lambda_l = \lambda_l^+ + \lambda_l^- \quad \text{and} \quad |\lambda_l| = \lambda_l^+ - \lambda_l^-. \tag{25}$$

The quasi-linear coupled equations are obtained from the characteristic form by the transformation matrix P (defined in [8]), with the Jacobian A satisfying

$$A = P\Lambda P^{-1}, \text{ resulting in } \partial Q/\partial t + A\partial Q/\partial x = 0. \tag{26}$$

Hence an upwind formulation can be obtained with the Jacobians

$$A^+ = P\Lambda^+ P^{-1} \quad \text{and} \quad A^- = P\Lambda^- P^{-1}, \tag{27}$$

$$\text{with: } A = A^+ + A^- \text{ and } |A| = A^+ - A^-. \tag{28}$$

The fluxes associated with these split Jacobians are obtained from the remarkable property of homogeneity of the flux vector *f(Q)*. *f(Q)* is a homogeneous function of degree one of *Q*. Hence, $f = AQ$ and the following flux splitting can be defined:

$$f^+ = A^+ Q \quad \text{and} \quad f^- = A^- Q, \tag{29}$$

$$\text{with: } f = f^+ + f^-. \tag{30}$$

This flux vector splitting, based on Eq. (21), has been introduced by [4]. The split fluxes f^+ and f^- are also homogeneous functions of degree one in *Q*.

3.2 Arbitrary Meshes

In practical computations one deal mostly with arbitrary meshes, considering either in a finite volume approach or in a curvilinear coordinate system.

In both cases, the upwind characterization is based on the signs of the eigenvalues of the matrix

$$K^{(n)} = \vec{A} \bullet \vec{n} = An_x + Bn_y + Cn_z, \tag{31}$$

where *A*, *B* and *C* are the Jacobian matrices written to the Cartesian system.

The fluxes will be decomposed by their components

$$\tilde{F}^{(n)} = \tilde{\tilde{F}} \bullet \vec{n} = En_x + Fn_y + Gn_z \tag{32}$$

and separated into positive and negative parts according to the sign of the eigenvalues of $K^{(n)}$ as described above, considering the normal direction as a local coordinate direction.

For a general eigenvalue splitting, as Eq. (21), the normal flux projection, Eq. (32), is decomposed by a [4] flux splitting as

$$\tilde{F}_{\pm}^{(n)} = \frac{\rho}{2\gamma} \begin{Bmatrix} \alpha \\ \alpha u + a\left(\lambda_2^{\pm} - \lambda_3^{\pm}\right) n_x \\ \alpha v + a\left(\lambda_2^{\pm} - \lambda_3^{\pm}\right) n_y \\ \alpha w + a\left(\lambda_2^{\pm} - \lambda_3^{\pm}\right) n_z \\ \alpha \dfrac{u^2+v^2+w^2}{2} + a v_n \left(\lambda_2^{\pm} - \lambda_3^{\pm}\right) + a^2 \dfrac{\lambda_2^{\pm} + \lambda_3^{\pm}}{\gamma - 1} \end{Bmatrix}, \tag{33}$$

where the eigenvalues of the matrix *K* are defined as

$$\lambda_1 = \vec{v} \bullet \vec{n} \equiv v_n, \ \lambda_2 = \vec{v} \bullet \vec{n} + a \quad \text{and} \quad \lambda_3 = \vec{v} \bullet \vec{n} - a, \tag{34}$$

with $\vec{v}$ being the flow velocity vector, and ± sign indicates the positive or negative parts respectively. The parameter α is defined as

$$\alpha = 2(\gamma - 1)\lambda_1^{\pm} + \lambda_2^{\pm} + \lambda_3^{\pm}. \tag{35}$$

3.3 RHS Definition

The numerical scheme of [4] implemented in this work is based on a finite volume formulation, where the fluxes at interface are calculated as

$$\tilde{\tilde{F}}_{i,j-1/2,k} = \left(\tilde{\tilde{F}}^-_{i,j-1,k} + \tilde{\tilde{F}}^+_{i,j,k}\right) S_{i,j-1/2,k}; \tag{36}$$

$$\tilde{\tilde{F}}_{i+1/2,j,k} = \left(\tilde{\tilde{F}}^-_{i+1,j,k} + \tilde{\tilde{F}}^+_{i,j,k}\right) S_{i+1/2,j,k}; \tag{37}$$

$$\tilde{\tilde{F}}_{i,j+1/2,k} = \left(\tilde{\tilde{F}}^-_{i,j+1,k} + \tilde{\tilde{F}}^+_{i,j,k}\right) S_{i,j+1/2,k}; \tag{38}$$

$$\tilde{\tilde{F}}_{i-1/2,j,k} = \left(\tilde{\tilde{F}}^-_{i-1,j,k} + \tilde{\tilde{F}}^+_{i,j,k}\right) S_{i-1/2,j,k}; \tag{39}$$

$$\tilde{\tilde{F}}_{i,j,k-1/2} = \left(\tilde{\tilde{F}}^-_{i,j,k-1} + \tilde{\tilde{F}}^+_{i,j,k}\right) S_{i,j,k-1/2}; \tag{40}$$

$$\tilde{\tilde{F}}_{i,j,k+1/2} = \left(\tilde{\tilde{F}}^-_{i,j,k+1} + \tilde{\tilde{F}}^+_{i,j,k}\right) S_{i,j,k+1/2}, \tag{41}$$

where S is the flux area calculated at each interface according to the procedure described in [22-23].

The Right-Hand-Side (RHS) of the [4] scheme, necessaries to the resolution of the implicit scheme, is defined by:

$$RHS(SW)^n_{i,j,k} = -\Delta t_{i,j,k} \Big/ V_{i,j,k} \left(\widetilde{F}^n_{i,j-1/2,k} + \widetilde{F}^n_{i+1/2,j,k} + \widetilde{F}^n_{i,j+1/2,k} + \widetilde{F}^n_{i-1/2,j,k} + \widetilde{F}^n_{i,j,k-1/2} + \widetilde{F}^n_{i,j,k+1/2} \right). \quad (42)$$

The terms in brackets in the RHS are a sum of normal fluxes because the correct signal of these fluxes is considered in Eqs. (36) to (41) by the signal of the normal unity vector components.

To perform the time integration in the explicit case, necessaries to the viscous simulations, the following algorithm is applied:

$$Q^{(n+1)}_{i,j,k} = Q^n_{i,j,k} + RHS(SW)^n_{i,j,k} \quad (43)$$

The viscous vectors at the flux interface are obtained by arithmetical average between the primitive variables at the left and at the right states of the flux interface, as also arithmetical average of the primitive variable gradients also considering the left and the right states of the flux interface. The gradients of the primitive variables present in the viscous flux vectors are calculated employing the Green Theorem which considers that the gradient of a primitive variable is constant in the volume and that the volume integral which defines this gradient is replaced by a surface integral ([24]); For instance, to $\partial u/\partial x$:

$$\frac{\partial u}{\partial x} = \frac{1}{V}\int_V \frac{\partial u}{\partial x} dV = \frac{1}{V}\int_V u\left(\vec{n} \bullet d\vec{S}\right) = \frac{1}{V}\int_V u dS_x \cong \frac{1}{V_{i,j,k}} \Big[0.5\left(u_{i,j,k} + u_{i,j-1,k}\right) S_{x_{i,j-1/2,k}} + 0.5\left(u_{i,j,k} + u_{i+1,j,k}\right) S_{x_{i+1/2,j,k}} + 0.5\left(u_{i,j,k} + u_{i,j+1,k}\right) S_{x_{i,j+1/2,k}} + 0.5\left(u_{i,j,k} + u_{i-1,j,k}\right) S_{x_{i-1/2,j,k}} + 0.5\left(u_{i,j,k} + u_{i,j,k-1}\right) S_{x_{i,j,k-1/2}} + 0.5\left(u_{i,j,k} + u_{i,j,k+1}\right) S_{x_{i,j,k+1/2}} \Big]. \quad (44)$$

This version of the flux vector splitting algorithm of [4] is first order accurate in space. The second order version, with TVD properties, will be introduced in this scheme in Section 7.

4 [5] Algorithm

The approximation to the integral Equation (1) to a hexahedron finite volume yields an ordinary differential equation system with respect to time:

$$V_{i,j,k}\, dQ_{i,j,k} \big/ dt = -R_{i,j,k}, \quad (45)$$

with $R_{i,j,k}$ representing the neat flux (residual) of the conservation of mass, of linear momentum and of energy in the $V_{i,j,k}$ volume. The residual is calculated as:

$$R_{i,j,k} = R_{i+1/2,j,k} - R_{i-1/2,j,k} + R_{i,j+1/2,k} - R_{i,j-1/2,k} + R_{i,j,k+1/2} - R_{i,j,k-1/2}, \quad (46)$$

where $R_{i+1/2,j,k} = R^c_{i+1/2,j,k}$, in which "c" is related to the flow convective contribution.

The discrete convective flux calculated by the AUSM scheme ("Advection Upstream Splitting Method") can be interpreted as a sum involving the arithmetical average between the right (R) and the left (L) states of the (i+½,j,k) cell face, related to cells (i,j,k) and (i+1,j,k), respectively, multiplied by the interface Mach number, and a scalar dissipative term, as shown in [6]. Hence,

$$R_{i+1/2,j,k} = \left|S\right|_{i+1/2,j,k} \left(\frac{1}{2} M_{i+1/2,j,k} \left(\begin{bmatrix} \rho a \\ \rho a u \\ \rho a v \\ \rho a w \\ \rho a H \end{bmatrix}_L + \begin{bmatrix} \rho a \\ \rho a u \\ \rho a v \\ \rho a w \\ \rho a H \end{bmatrix}_R \right) - \frac{1}{2} \phi_{i+1/2,j,k} \left(\begin{bmatrix} \rho a \\ \rho a u \\ \rho a v \\ \rho a w \\ \rho a H \end{bmatrix}_R - \begin{bmatrix} \rho a \\ \rho a u \\ \rho a v \\ \rho a w \\ \rho a H \end{bmatrix}_L \right) \right) + \begin{bmatrix} 0 \\ S_x p \\ S_y p \\ S_z p \\ 0 \end{bmatrix}_{i+1/2,j,k}, \quad (47)$$

where $S_{i+1/2,j,k} = \begin{bmatrix} S_x & S_y & S_z \end{bmatrix}^T_{i+1/2,j,k}$ defines the normal area vector to the (i+½,j,k) surface. The "a" quantity represents the speed of sound, calculated as $a = \sqrt{\gamma p/\rho}$. $M_{i+½,j,k}$ defines the advective Mach number at the (i+½,j,k) face of the cell (i,j,k), which is calculated according to [6] as:

$$M_{i+1/2,j,k} = M^+_L + M^-_R, \quad (48)$$

where the $M^{+/-}$ separated Mach numbers are defined by [5] as:

$$M^{+} = \begin{cases} M, & if\ M \geq 1; \\ 0.25(M+1)^2, & if\ |M| < 1; \\ 0, & if\ M \leq -1; \end{cases} \quad (49)$$

$$M^{-} = \begin{cases} 0, & if\ M \geq 1; \\ -0.25(M-1)^2, & if\ |M| < 1; \\ M, & if\ M \leq -1. \end{cases} \quad (50)$$

M_L and M_R represent the Mach numbers associated to the left and right states, respectively. The advection Mach number is defined as:

$$M = \left(S_x u + S_y v + S_z w\right) / \left(a|S|\right). \quad (51)$$

The pressure at the (i+½,j,k) face of the (i,j,k) cell is calculated from a similar way:

$$p_{i+1/2,j,k} = p_L^{+} + p_R^{-}, \quad (52)$$

with $p^{+/-}$ representing the pressure separation defined according to [5]:

$$p^{+} = \begin{cases} p, & if\ M \geq 1; \\ 0.25p(M+1)^2(2-M), & if\ |M| < 1; \\ 0, & if\ M \leq -1; \end{cases} \quad (53)$$

$$p^{-} = \begin{cases} 0, & if\ M \geq 1; \\ 0.25p(M-1)^2(2+M), & if\ |M| < 1; \\ p, & if\ M \leq -1. \end{cases} \quad (54)$$

The definition of the ϕ dissipation term determines the particular formulation to the convective fluxes. The following choice corresponds to the [5] scheme, according to[7]:

$$\phi_{i+1/2,j,k} = \phi^{VL}_{i+1/2,j,k} = \begin{cases} |M_{i+1/2,j,k}|, & if\ |M_{i+1/2,j,k}| \geq 1; \\ |M_{i+1/2,j,k}| + 0.5(M_R - 1)^2, & if\ 0 \leq M_{i+1/2,j,k} < 1; \\ |M_{i+1/2,j,k}| + 0.5(M_L + 1)^2, & if\ -1 < M_{i+1/2,j,k} \leq 0. \end{cases} \quad (55)$$

The right-hand-side of the [5] scheme, necessaries to the implicit resolution of this algorithm, is defined as:

$$RHS(VL)^n_{i,j,k} = -\Delta t_{i,j,k} / V_{i,j,k} \left(R^n_{i+1/2,j,k} - R^n_{i-1/2,j,k} + R^n_{i,j+1/2,k} - R^n_{i,j-1/2,k} + R^n_{i,j,k+1/2} - R^n_{i,j,k-1/2} \right). \quad (56)$$

The terms in brackets at the RHS are a sum of differences of normal fluxes because the correct signal of these fluxes is not completely considered in Eq. (47), requiring that the correct signal should be considered explicitly.

To the viscous simulations, it is necessary to implement the explicit version. In this case, the time integration is accomplished by a dimensional splitting method, first order accurate, which divides the temporal integration in three steps, each one associated with a different spatial direction (in each direction is solved an one-dimensional problem by applying an one-dimensional operator). Considering the initial step associated with the ξ direction, one has:

$$\Delta Q^{*}_{i,j,k} = -\Delta t_{i,j,k} / V_{i,j,k} \left(F^n_{i+1/2,j,k} - F^n_{i-1/2,j,k} \right);$$

$$Q^{*}_{i,j,k} = Q^n_{i,j,k} + \Delta Q^{*}_{i,j,k}; \quad (57)$$

In the intermediate step, considering the η direction, one has:

$$\Delta Q^{**}_{i,j,k} = -\Delta t_{i,j,k} / V_{i,j,k} \left(F^{*}_{i,j+1/2,k} - F^{*}_{i,j-1/2,k} \right);$$

$$Q^{**}_{i,j,k} = Q^{*}_{i,j,k} + \Delta Q^{**}_{i,j,k}; \quad (58)$$

And, in the final step, considering the ζ direction, one has:

$$\Delta Q^{n+1}_{i,j,k} = -\Delta t_{i,j,k} / V_{i,j,k} \left(F^{**}_{i,j,k+1/2} - F^{**}_{i,j,k-1/2} \right);$$

$$Q^{n+1}_{i,j,k} = Q^{**}_{i,j,k} + \Delta Q^{n+1}_{i,j,k}, \quad (59)$$

where F, F^{*} and F^{**} incorporate the convective and the diffusive contributions. In other words, the viscous vectors at the flux interface are subtracted from the respective convective contributions. They are obtained from the same procedure described in section 3.

This version of the [5] scheme is first order accurate in space. The second order version, with TVD properties, will be introduced in this scheme in Section 7.

5 [6] Algorithm

The [6] scheme is described by the Eqs. (45) to (54). The next step is the determination of the ϕ dissipative term. The following choice corresponds to the [6] scheme, according to [7]:

$$\phi_{i+1/2,j,k} = \phi^{LS}_{i+1/2,j,k} = \left|M_{i+1/2,j,k}\right|. \qquad (60)$$

The right-hand-side of the [6] scheme, necessaries to the implicit resolution of this algorithm, is defined as:

$$RHS(LS)^n_{i,j,k} = -\Delta t_{i,j,k}/V_{i,j,k}\left(R^n_{i+1/2,j,k} - R^n_{i-1/2,j,k} + R^n_{i,j+1/2,k} - R^n_{i,j-1/2,k} + R^n_{i,j,k+1/2} - R^n_{i,j,k-1/2}\right). \qquad (61)$$

The terms in brackets at the RHS are a sum of differences of normal fluxes because the correct signal of these fluxes is not completely considered in Eq. (47), requiring that the correct signal should be considered explicitly.

The explicit version of this algorithm to perform the viscous simulations is described by Eqs. (57) to (59). The viscous vectors at the flux interface are subtracted from the respective convective contributions, Eq. (47), and are obtained from the same procedure described in section 3.

This version of the [6] scheme is first order accurate in space. The second order version, with TVD properties, will be introduced in this scheme in Section 7.

6 [7] Algorithm

The [7] scheme is described by the Eqs. (45) to (54). The next step is the determination of the ϕ dissipative term. A hybrid scheme is proposed by [7], which combines the [5] scheme and the [6] (AUSM) scheme. Hence,

$$\phi_{i+1/2,j} = (1-\omega)\phi^{VL}_{i+1/2,j} + \omega\,\phi^{LS}_{i+1/2,j}, \qquad (62)$$

with:

$$\phi^{VL}_{i+1/2,j,k} = \begin{cases} \left|M_{i+1/2,j,k}\right|, & if\ \left|M_{i+1/2,j,k}\right| \geq 1; \\ \left|M_{i+1/2,j,k}\right| + \frac{1}{2}(M_R - 1)^2, & if\ 0 \leq M_{i+1/2,j,k} < 1; \\ \left|M_{i+1/2,j,k}\right| + \frac{1}{2}(M_L + 1)^2, & if\ -1 < M_{i+1/2,j,k} \leq 0; \end{cases} \qquad (63)$$

$$\phi^{LS}_{i+1/2,j,k} = \begin{cases} \left|M_{i+1/2,j.k}\right|, & if\ \left|M_{i+1/2,j,k}\right| > \tilde{\delta} \\ \dfrac{\left(M_{i+1/2,j.k}\right)^2 + \tilde{\delta}^2}{2\tilde{\delta}}, & if\ \left|M_{i+1/2,j,k}\right| \leq \tilde{\delta}, \end{cases} \qquad (64)$$

where $\tilde{\delta}$ is a small parameter, $0 < \tilde{\delta} \leq 0.5$, and ω is a constant, $0 \leq \omega \leq 1$. In this work, the values used to $\tilde{\delta}$ and ω were: 0.2 and 0.5, respectively. The right-hand-side of the [7] scheme, necessaries to the implicit resolution of this algorithm, is defined as:

$$RHS(RK)^n_{i,j,k} = -\Delta t_{i,j,k}/V_{i,j,k}\left(R^n_{i+1/2,j,k} - R^n_{i-1/2,j,k} + R^n_{i,j+1/2,k} - R^n_{i,j-1/2,k} + R^n_{i,j,k+1/2} - R^n_{i,j,k-1/2}\right) \qquad (65)$$

The terms in brackets at the RHS are a sum of differences of normal fluxes because the correct signal of these fluxes is not completely considered in Eq. (47), requiring that the correct signal should be considered explicitly.

The explicit version of this algorithm to perform the viscous simulations is described by Eqs. (57) to (59). The viscous vectors at the flux interface are subtracted from the respective convective contributions, Eq. (47), and are obtained from the same procedure described in section 3.

This version of the [7] scheme is first order accurate in space. The second order version, with TVD properties, will be introduced in this scheme in Section 7.

7 Second Order Accuracy / MUSCL Approach

Second order spatial accuracy can be achieved by introducing more upwind points or cells in the schemes. It has been noted that the projection stage, whereby the solution is projected in each cell face (i-1/2,j,k; i+1/2,j,k) on piecewise constant states, is the cause of the first order space accuracy of the Godunov schemes ([8]). Hence, it is sufficient to modify the first projection stage without modifying the Riemann solver, in order to generate higher spatial approximations. The state variables at the interfaces are thereby obtained from an extrapolation between neighboring cell averages. This method for the generation of second order upwind schemes based on variable extrapolation is often referred to in the literature as the MUSCL ("Monotone Upstream-centered Schemes for

Conservation Laws") approach. The use of nonlinear limiters in such procedure, with the intention of restricting the amplitude of the gradients appearing in the solution, avoiding thus the formation of new extrema, allows that first order upwind schemes be transformed in TVD high resolution schemes with the appropriate definition of such nonlinear limiters, assuring monotone preserving and total variation diminishing methods. Details of the present implementation of the MUSCL procedure, as well the incorporation of TVD properties to the schemes, are found in [8]. The expressions to calculate de fluxes following a MUSCL procedure and the nonlinear flux limiter definitions employed in this work, which incorporates TVD properties, are defined as follows.

The conserved variables at the interface (i+½,j,k) can be considered as resulting from a combination of backward and forward extrapolations. To a linear one-sided extrapolation at the interface between the averaged values at the two upstream cells (i,j,k) and (i-1,j,k), one has:

$$Q^{L}_{i+1/2,j,k} = Q_{i,j,k} + \frac{\varepsilon}{2}\left(Q_{i,j,k} - Q_{i-1,j,k}\right), \text{ cell (i,j);} \quad (66)$$

$$Q^{R}_{i+1/2,j,k} = Q_{i+1,j,k} - \frac{\varepsilon}{2}\left(Q_{i+2,j,k} - Q_{i+1,j,k}\right), \text{ cell (i+1,j,k),} \quad (67)$$

leading to a second order fully one-sided scheme. If the first order scheme is defined by the numerical flux

$$F_{i+1/2,j,k} = F\left(Q_{i,j,k}, Q_{i+1,j,k}\right) \quad (68)$$

the second order space accurate numerical flux is obtained from

$$F^{(2)}_{i+1/2,j,k} = F\left(Q^{L}_{i+1/2,j,k}, Q^{R}_{i+1/2,j,k}\right). \quad (69)$$

Higher order flux vector splitting or flux difference splitting methods, such as those studied in this work, are obtained from:

$$F^{(2)}_{i+1/2,j,k} = F^{+}\left(Q^{L}_{i+1/2,j,k}\right) + F^{-}\left(Q^{R}_{i+1/2,j,k}\right). \quad (70)$$

All second order upwind schemes necessarily involve at least five mesh points or cells. To reach high order solutions without oscillations around discontinuities, nonlinear limiters are employed, replacing the term ε in Eqs. (66) and (67) by these limiters at the left and at the right states of the flux interface. To define such limiters, it is necessary to calculate the ratio of consecutive variations of the conserved variables. These ratios are defined as follows:

$$r^{+}_{i-1/2,j,k} = \left(Q_{i+1,j,k} - Q_{i,j,k}\right) / \left(Q_{i,j,k} - Q_{i-1,j,k}\right); \quad (71)$$

$$r^{+}_{i+1/2,j,k} = \left(Q_{i+2,j,k} - Q_{i+1j,k}\right) / \left(Q_{i+1,j,k} - Q_{i,j,k}\right), \quad (72)$$

where the nonlinear limiters at the left and at the right states of the flux interface are defined by $\Psi^{L} = \Psi\left(r^{+}_{i-1/2,j,k}\right)$ and $\Psi^{R} = \Psi\left(1/r^{+}_{i+1/2,j,k}\right)$. In this work, five options of nonlinear limiters were considered to the numerical experiments. These limiters are defined as follows:

$$\Psi^{VL}_{l}(r_l) = \frac{r_l + |r_l|}{1 + r_l}, \text{ [25] limiter;} \quad (73)$$

$$\Psi^{VA}_{l}(r_l) = \frac{r_l + r_l^2}{1 + r_l^2}, \text{ Van Albada limiter;} \quad (74)$$

$$\Psi^{MIN}_{l}(r_l) = signal_l\, MAX\left(0, MIN\left(|r_l|, signal_l\right)\right), \text{ named minmod limiter;} \quad (75)$$

$$\Psi^{SB}_{l}(r_l) = MAX\left(0, MIN\left(2r_l, 1\right), MIN\left(r_l, 2\right)\right), \text{ named "Super Bee" limiter, due to [26];} \quad (74)$$

$$\Psi^{\beta-L}_{l}(r_l) = MAX\left(0, MIN\left(\beta r_l, 1\right), MIN\left(r_l, \beta\right)\right), \quad \beta\text{-limiter,} \quad (75)$$

with "*l*" varying from 1 to 5 (three-dimensional space), $signal_l$ being equal to 1.0 if $r_l \geq 0.0$ and -1.0 otherwise, r_l is the ratio of consecutive variations of the *l*th conserved variable and β is a parameter assuming values between 1.0 and 2.0, being 1.5 the value assumed in this work. With the implementation of the numerical flux vectors following this MUSCL procedure, second order spatial accuracy and TVD properties are incorporated in the algorithms.

8 Implicit Formulation

All implicit schemes implemented in this work used backward Euler in time and ADI approximate factorization to solve a three-diagonal system in each direction.

The ADI approximate factorization form to the implicit schemes of [4-7] is presented in three

stages, each one associated with a different coordinate direction:

$$\left[I+\Delta t_{i,j,k}\Delta_{+}^{\xi}A_{i+1/2,j,k}^{-}+\Delta t_{i,j,k}\Delta_{-}^{\xi}A_{i+1/2,j,k}^{+}\right]\Delta Q_{i,j,k}^{*}=RHS_{i,j,k}\,; \quad (76)$$

$$\left[I+\Delta t_{i,j,k}\Delta_{+}^{\eta}B_{i,j+1/2,k}^{-}+\Delta t_{i,j,k}\Delta_{-}^{\eta}B_{i,j+1/2,k}^{+}\right]\Delta Q_{i,j,k}^{**}=\Delta Q_{i,j,k}^{*}\,; \quad (77)$$

$$\left[I+\Delta t_{i,j,k}\Delta_{+}^{\xi}C_{i,j,k+1/2}^{-}+\Delta t_{i,j,k}\Delta_{-}^{\zeta}C_{i,j,k+1/2}^{+}\right]\Delta Q_{i,j,k}^{n+1}=\Delta Q_{i,j,k}^{**}\,, \quad (78)$$

where: $RHS_{i,j,k}$ is defined by Eq. (42) or (56) or (61) or (65) depending if the [4] or the [5] or the [6] or the [7] scheme is being solved, respectively; the difference operators are defined as:

$$\Delta_{+}^{\xi}(\cdot)=(\cdot)_{i+1,j,k}-(\cdot)_{i,j,k}\,,\ \Delta_{-}^{\xi}(\cdot)=(\cdot)_{i,j,k}-(\cdot)_{i-1,j,k}\,; \quad (79)$$

$$\Delta_{+}^{\eta}(\cdot)=(\cdot)_{i,j+1,k}-(\cdot)_{i,j,k}\,; \quad (80)$$

$$\Delta_{-}^{\eta}(\cdot)=(\cdot)_{i,j,k}-(\cdot)_{i,j-1,k}\,,\ \Delta_{+}^{\zeta}(\cdot)=(\cdot)_{i,j,k+1}-(\cdot)_{i,j,k}\,; \quad (81)$$

$$\Delta_{-}^{\zeta}(\cdot)=(\cdot)_{i,j,k}-(\cdot)_{i,j,k-1}\,. \quad (82)$$

and the update of the conserved variable vector is proceeded as follows:

$$Q_{i,j,k}^{n+1}=Q_{i,j,k}^{n}+\Delta Q_{i,j,k}^{n+1}\,. \quad (83)$$

This system of 5x5 block three-diagonal linear equations is solved using LU decomposition and the Thomas algorithm applied to systems of block matrices.

The splitting matrices A^+, A^-, B^+, B^-, C^+ and C^- are defined as:

$$A^{+}=T_{\xi}\Lambda_{\xi}^{+}T_{\xi}^{-1}\,,\ A^{-}=T_{\xi}\Lambda_{\xi}^{-}T_{\xi}^{-1}\,,\ B^{+}=T_{\eta}\Lambda_{\eta}^{+}T_{\eta}^{-1}\,; \quad (84)$$

$$B^{-}=T_{\eta}\Lambda_{\eta}^{-}T_{\eta}^{-1}\,,\ C^{+}=T_{\zeta}\Lambda_{\zeta}^{+}T_{\zeta}^{-1}\,,\ C^{-}=T_{\zeta}\Lambda_{\zeta}^{-}T_{\zeta}^{-1}\,, \quad (85)$$

where the similar transformation matrix T and its inverse are specified in [23]. The diagonal matrices of eigenvalues are given, for instance, by:

$$\Lambda_{\xi}^{+}=\begin{bmatrix}\lambda_1^{\xi,+} & & & & \\ & \lambda_2^{\xi,+} & & & \\ & & \lambda_3^{\xi,+} & & \\ & & & \lambda_4^{\xi,+} & \\ & & & & \lambda_5^{\xi,+}\end{bmatrix}; \quad (86)$$

$$\Lambda_{\xi}^{-}=\begin{bmatrix}\lambda_1^{\xi,-} & & & & \\ & \lambda_2^{\xi,-} & & & \\ & & \lambda_3^{\xi,-} & & \\ & & & \lambda_4^{\xi,-} & \\ & & & & \lambda_5^{\xi,-}\end{bmatrix}; \quad (87)$$

with the eigenvalues of the Euler equations in the ξ, η and ζ directions, normal to the respective cell faces, evaluated by:

$$v_n=u_{\mathrm{int}}h_x+v_{\mathrm{int}}h_y+w_{\mathrm{int}}h_z\,,\ \lambda_1=v_n\,,\ \lambda_2=v_n\,; \quad (88)$$

$$\lambda_3=v_n\,,\ \lambda_4=v_n+a_{\mathrm{int}}h_n\,,\ \lambda_5=v_n-a_{\mathrm{int}}h_n\,, \quad (89)$$

where the metric terms defined in [23], and the eigenvalue splitting defined according to [4], using Eq. (21). This implicit formulation to the Left-Hand-Side (LHS) of [4-7] schemes is first order accurate in time and space. As the steady state condition is the desirable solution, the spatial solution accuracy is determined by the RHS accuracy, which is second order with the MUSCL implementation in all schemes, since the LHS tends to zero in the steady condition.

9 Turbulence Models

9.1 Turbulence Model of [14]

The problem of the turbulent simulation is in the calculation of the Reynolds stress. Expressions involving velocity fluctuations, originating from the averaging process, represent six new unknowns. However, the number of equations keeps the same and the system is not closed. The modeling function is to develop approximations to these correlations. To the calculation of the turbulent viscosity according to the [14] model, the boundary layer is divided in internal and external.

Initially, the (ν_w) kinematic viscosity at wall and the ($\tau_{xy,w}$) shear stress at wall are calculated. After that, the (δ) boundary layer thickness, the (δ_{LM}) linear momentum thickness and the (Vt_{BL}) boundary layer tangential velocity are calculated. So, the (N) normal distance from the wall to the studied cell is calculated. The N^+ term is obtained from:

$$N^{+}=\sqrt{\mathrm{Re}}\sqrt{\tau_{xy,w}/\rho_w}\;N/\nu_w\,, \quad (90)$$

where ρ_w is the wall density. The van Driest damping factor is calculated by:

$$D = 1 - e^{(-N^+\sqrt{\rho/\rho_w}\mu_w/\mu/A^+)}, \quad (91)$$

with $A^+ = 26$ and μ_w is the wall molecular viscosity. After that, the (dVt/dN) normal to the wall gradient of the tangential velocity is calculated and the internal turbulent viscosity is given by:

$$\mu_{Ti} = \mathrm{Re}\rho(\kappa ND)^2\, dVt/dN, \quad (92)$$

where κ is the von Kárman constant, which has the value 0.4. The intermittent function of Klebanoff is calculated to the external viscosity by:

$$g_{Kleb}(N) = \left[1 + 5.5(N/\delta)^6\right]^{-1}. \quad (93)$$

With it, the external turbulent viscosity is calculated by:

$$\mu_{Te} = \mathrm{Re}(0.0168)\rho Vt_{BL}\delta_{LM} g_{Kleb}. \quad (94)$$

Finally, the turbulent viscosity is chosen from the internal and the external viscosities: $\mu_T = MIN(\mu_{Ti}, \mu_{Te})$.

9.2 Turbulence Model of [15]

To the calculation of the turbulent viscosity according to the [15] model, the boundary layer is again divided in internal and external. In the internal layer,

$$\mu_{Ti} = \rho l_{mix}^2 \|\omega\| \quad \text{and} \quad l_{mix} = \kappa N\left(1 - e^{-N^+/A_0^+}\right). \quad (95)$$

In the external layer,

$$\mu_{Te} = \rho\alpha C_{cp} F_{wake} F_{Kleb}(N; N_{\max}/C_{Kleb}), \quad (96)$$

with:

$$F_{wake} = MIN\left[N_{\max} F_{\max}; C_{wk} N_{\max} U_{dif}^2 / F_{\max}\right]; \quad (97)$$

$$F_{\max} = 1/\kappa\left[\underset{N}{MAX}\left(l_{mix}\|\omega\|\right)\right]. \quad (98)$$

Hence, $N_{\max}$ is the value of N where $l_{mix}\|\omega\|$ reached its maximum value and l_{mix} is the Prandtl mixture length. The constant values are: $\kappa = 0.4$, $\alpha = 0.0168$, $A_0^+ = 26$, $C_{cp} = 1.6$, $C_{Kleb} = 0.3$ and $C_{wk} = 1$. F_{Kleb} is the intermittent function of Klebanoff given by:

$$F_{Kleb}(N) = \left[1 + 5.5(C_{Kleb} N/N_{\max})^6\right]^{-1}, \quad (99)$$

$\|\omega\|$ is the magnitude of the vorticity vector and U_{dif} is the maximum velocity value in the boundary layer case. To free shear layers,

$$U_{dif} = \left(\sqrt{u^2 + v^2 + w^2}\right)_{\max} - \left(\sqrt{u^2 + v^2 + w^2}\right)_{N=N_{\max}}. \quad (100)$$

10 Spatially Variable Time Step

The idea of a spatially variable time step consists in keeping constant a CFL number in the calculation domain and to guarantee time steps appropriated to each mesh region during the convergence process. The spatially variable time step can be defined by:

$$\Delta t_{i,j,k} = \frac{CFL(\Delta s)_{i,j,k}}{(|q| + a)_{i,j,k}}, \quad (101)$$

where CFL is the Courant-Friedrichs-Lewis number to method stability; $(\Delta s)_{i,j,k}$ is a characteristic length of information transport; and $(|q| + a)_{i,j,k}$ is the maximum characteristic speed of information transport, where a is the speed of sound. The characteristic length of information transport, $(\Delta s)_{i,j,k}$, can be determined by:

$$(\Delta s)_{i,j,k} = \left[MIN(l_{MIN}, C_{MIN})\right]_{i,j,k}, \quad (102)$$

where l_{MIN} is the minimum side length which forms a computational cell and C_{MIN} is the minimum distance of baricenters among the computational cell and its neighbors. The maximum characteristic speed of information transport is defined by $(|q| + a)_{i,j,k}$, with $q = \sqrt{u^2 + v^2 + w^2}$.

11 Initial and Boundary Conditions

11.1 Initial Conditions

The initial condition adopted for the problems is the freestream flow in all calculation domain ([18, 27]). The vector of conserved variables is expressed as follows:

$$Q_\infty = \left\{1 \quad M_\infty\cos\theta \quad M_\infty\sin\theta\cos\psi \quad M_\infty\sin\theta\sin\psi \quad \left[\frac{1}{\gamma(\gamma-1)} + \frac{M_\infty^2}{2}\right]\right\}^t, \quad (103)$$

where M_∞ represents the freestream Mach number, θ is the flow incidence angle upstream the

configuration under study and ψ is the angle in the configuration longitudinal plane.

11.2 Boundary Conditions

The different types of implemented boundary conditions are described as follows. They are implemented in special cells named "ghost cells", as referred in the Computational Fluid Dynamics (CFD) community.

a) Wall condition - The Euler case requires the flux tangency condition. On the context of finite volumes, this imposition is done considering that the tangent flow velocity component to the wall of the ghost cell be equal to the tangent flow velocity component to the wall of the neighbor real cell. At the same time, the normal flow velocity component to the wall of the ghost cell should be equal to the negative of the normal flow velocity component to the wall of the neighbor real cell. [28] suggests that these procedures lead to the following expressions to the velocity components *u*, *v* and *w* of the ghost cells:

$$u_g = (1-2n_x n_x)u_{real} + (-2n_x n_y)v_{real} + (-2n_x n_z)w_{real}; \quad (104)$$

$$v_g = (-2n_y n_x)u_{real} + (1-2n_y n_y)v_{real} + (-2n_y n_z)w_{real}; \quad (105)$$

$$w_g = (-2n_z n_x)u_{real} + (-2n_z n_y)v_{real} + (1-2n_z n_z)w_{real}. \quad (106)$$

In the viscous case, however, the velocity components of the ghost cells are set equal to corresponding values of the velocity components of the real neighbor, with opposite signal. In other words:

$$u_g = -u_{real},\ v_g = -v_{real} \quad \text{and} \quad w_g = -w_{real}. \quad (107)$$

The fluid pressure gradient in the direction normal to the wall is equal to zero for the inviscid case and also equaled to zero in the viscous case due to the boundary layer theory. The temperature gradient is equal to zero along the whole wall, according to the condition of adiabatic wall, for both cases (viscous and non-viscous). With these two conditions, a zero order extrapolation is performed to the fluid pressure and to the temperature. It is possible to conclude that the fluid density will also be obtained by zero order extrapolation. The energy conserved variable is obtained from the state equation to a perfect gas, Eq. (17).

b) Entrance Condition:

b.1) Entrance with subsonic flow – Considering the one-dimensional characteristic relation concept in the normal direction of flow penetration, the entrance with subsonic flow presents four characteristic velocities of information propagation which have direction and orientation pointing inward the calculation domain, which implies that the variables associated with these waves cannot be extrapolated ([27]). It is necessary to specify four conditions to these four information. [18] indicate as appropriated quantities to be specified the freestream density and the freestream Cartesian velocity components *u*, *v* and *w*. Just the last characteristics, "(q_n-a)", which transports information from inside to outside of the calculation domain, cannot be specified and will have to be determined by interior information of the calculation domain. In this work, a zero order extrapolation to the pressure is performed, being the total energy defined by the state equation of a perfect gas.

b.2) Entrance with supersonic flow - All variables are specified at the entrance boundary, adopting freestream values.

c) Exit Condition:

c.1) Exit with subsonic flow - Four characteristics which govern the Euler equations proceed from the internal region of the calculation domain. So, the density and the Cartesian velocity components are extrapolated from the interior domain ([27]). One condition should be specified to the boundary. In this case, the pressure is fixed in the calculation domain exit, keeping its respective value of freestream flow. Total energy is specified by the equation of state to a perfect gas.

c.2) Exit with supersonic flow - The five characteristics which govern the Euler equations proceed from the internal region of the calculation domain. It is not possible to specify variable values at the exit. The zero order extrapolation is applied to density, Cartesian velocity components and pressure. Total energy is specified by the equation of state to a perfect gas.

12 Results

Tests were performed in a microcomputer with processor AMD SEMPRON (tm) 2600+, 1.83GHz, and 512 Mbytes of RAM memory. As the interest of this work is steady state problems, one needs to define a criterion which guarantees that such condition was reached. The criterion adopted in this work was to consider a reduction of 3 orders in the

magnitude of the maximum residual in the domain, a typical criterion in the CFD community. The residual to each cell was defined as the numerical value obtained from the discretized conservation equations. As there are five conservation equations to each cell, the maximum value obtained from these equations is defined as the residual of this cell. Thus, this residual is compared with the residual of the others cells, calculated of the same way, to define the maximum residual in the domain. The configuration upstream and the configuration longitudinal plane angles were set equal to 0.0°. All pressure distributions were determined at the plane corresponding to k = KMAX/2, where "KMAX" is the maximum number of points in the z direction, and j = 1, corresponding to the configuration wall.

To the inviscid case, the implicit formulation was employed to generate the numerical results, whereas to the viscous laminar and turbulent cases, the explicit version of the numerical algorithms was used.

12.1 Inviscid Results

A freestream Mach number of 3.0, characterizing a supersonic flow regime, was adopted as initial condition to the compression corner problem. The flow reaches the compression corner, generating an oblique shock wave along the corner.

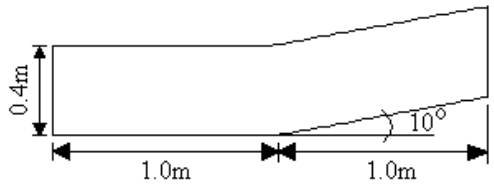

Figure 1. Corner configuration in the xy plane.

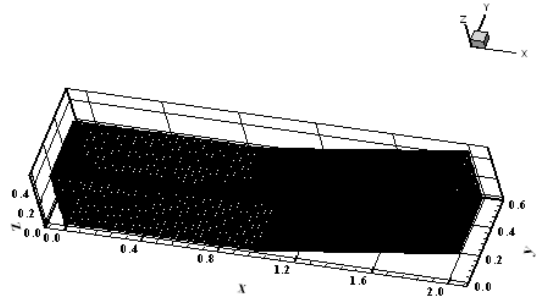

Figure 2. Corner mesh in three-dimensions.

The compression corner configuration at the xy plane is described in Fig. 1. The corner inclination angle is 10^o. An algebraic mesh of 70 points in the ξ direction, 50 points in the η direction and 10 points in the ζ direction was generated, which corresponds in finite volumes to 30,429 hexahedrons and 35,000 nodes. Its spanwise length is 0.50m. Figure 2 exhibits such mesh.

Figures 3 to 8 exhibit the pressure contours obtained by the scheme of [4] in its three variants, corresponding to the three limiters employed in this study: VL (Van Leer), VA (Van Albada) and Min (*minmod*).

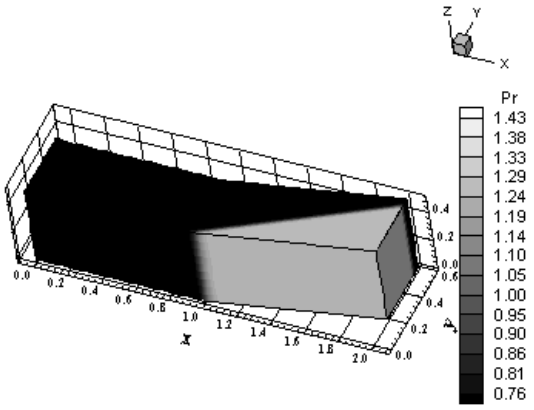

Figure 3. Pressure contours ([4]-VL).

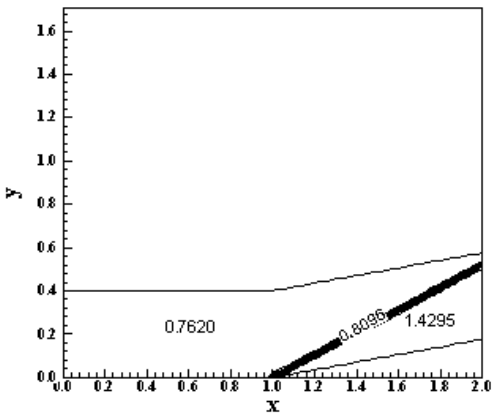

Figure 4. Pressure contours ([4]-VL).

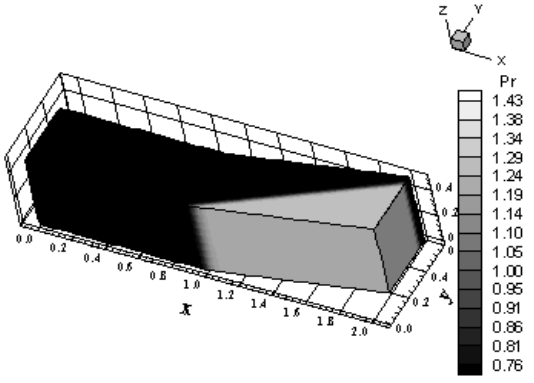

Figure 5. Pressure contours ([4]-VA).

Figures 3 and 4 show the pressure contours obtained by the [4] TVD scheme, using the VL limiter, in three-dimensions and at the xy plane (k = 1), respectively. Figures 5 and 6 present the pressure contours obtained by the [4] TVD scheme, using VA limiter, in three-dimensions and at the xy plane (k = 1), respectively.

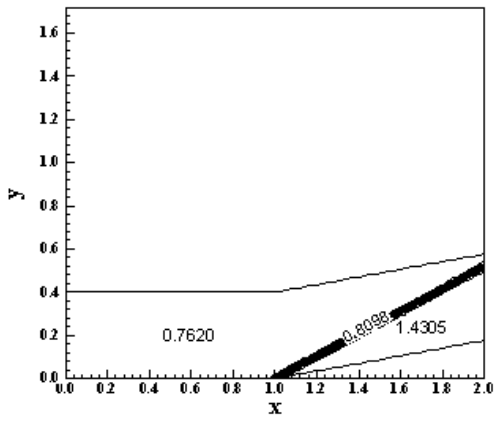

Figure 6. Pressure contours ([4]-VA).

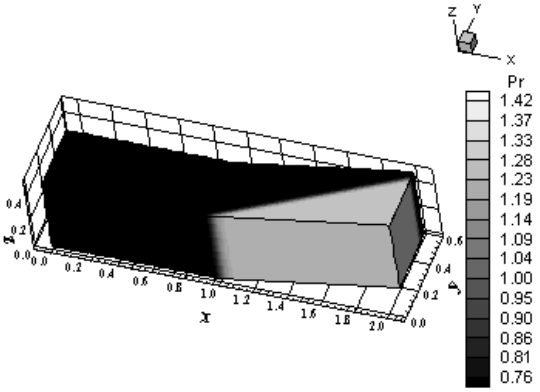

Figure 7. Pressure contours ([4]-Min).

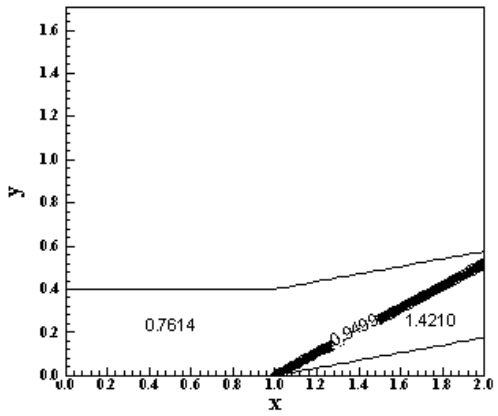

Figure 8. Pressure contours ([4]-Min).

Finally, Figures 7 and 8 exhibit the pressure contours obtained by the [4] TVD scheme, using Min limiter, in three-dimensions and at the xy plane (k = 1), respectively. As can be observed, the most intense pressure field was obtained by the [4] TVD scheme using VA limiter.

Figure 9 shows the wall pressure distributions obtained by the three variants of the [4] TVD scheme. They are compared with the oblique shock wave theory. As can be observed, all solutions present good pressure distributions, capturing the shock discontinuity in three cells, which is an excellent result in terms of high resolution schemes. The best wall pressure distribution involving the [4] TVD variants is due to the Min limiter.

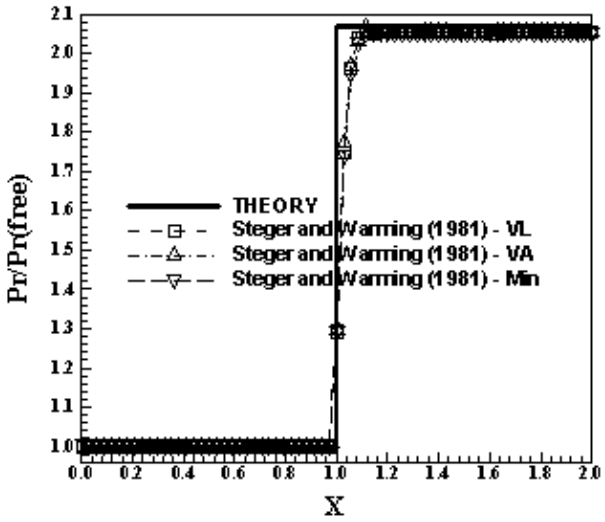

Figure 9. Wall pressure distributions ([4]).

One way to quantitatively verify if the solutions generated by each variant of the [4] TVD scheme are satisfactory consists in determining the shock angle of the oblique shock wave, β, measured in relation to the initial direction of the flow field. [29] (pages 352 and 353) presents a diagram with values of the shock angle, β, to oblique shock waves.

Table 1. Shock angle of the oblique shock wave at the compression corner and percentage error ([4]).

Scheme	β (°)	Error (%)
[4]-VL	27.6	0.36
[4]-VA	27.9	1.45
[4]-Min	27.7	0.73

The value of this angle is determined as function of the freestream Mach number and of the deflection angle of the flow after the shock wave, ϕ. To the compression corner problem, ϕ = 10º (ramp

inclination angle) and the freestream Mach number is 3.0, resulting from this diagram a value to β equals to 27.5º. Using a transfer in Figures 4, 6 and 8, it is possible to obtain the values of β to each variant of the [4] TVD scheme, as well the respective errors, shown in Tab. 1. As can be observed, the best variant was the [4] TVD scheme using VL limiter, with a percentage error of 0.36%.

Figures 10 to 15 exhibit the pressure contours obtained by the scheme of [5] in its three variants: VL, VA and Min. Figures 10 and 11 show the pressure contours obtained by the [5] TVD scheme, using the VL limiter, in three-dimensions and at the xy plane, respectively. Figures 12 and 13 present the pressure contours obtained by the [5] TVD scheme, using VA limiter, in three-dimensions and at the xy plane, respectively. Finally, Figures 14 and 15 exhibit the pressure contours obtained by the [5] TVD scheme, using Min limiter, in three-dimensions and at the xy plane, respectively. As can be observed, the most intense pressure field was obtained by the [5] TVD scheme using VL limiter.

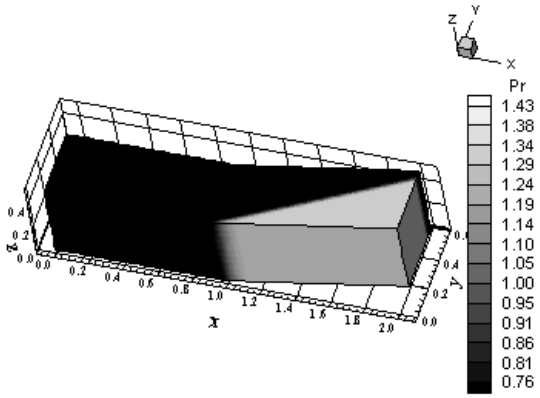

Figure 10. Pressure contours ([5]-VL).

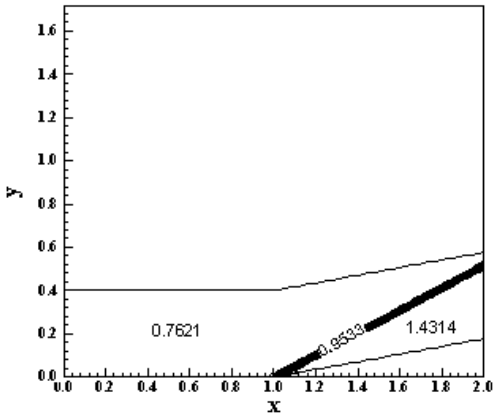

Figure 11. Pressure contours ([5]-VL).

Figure 16 shows the wall pressure distributions obtained by the three variants of the [5] TVD scheme. They are compared with the oblique shock wave theory. As can be observed, all solutions present good pressure distributions, capturing the shock discontinuity in four cells, which is a reasonable result in terms of high resolution schemes. The best wall pressure distribution involving the [5] TVD variants is due to the Min limiter.

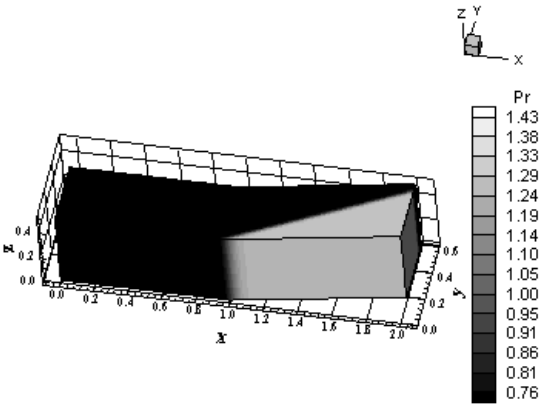

Figure 12. Pressure contours ([5]-VA).

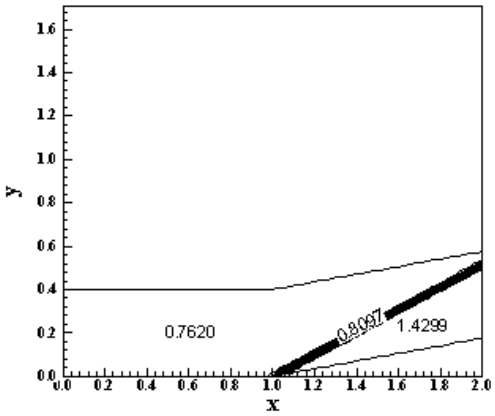

Figure 13 : Pressure contours ([5]-VA).

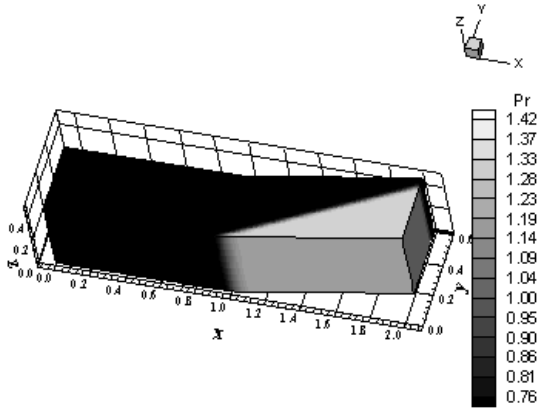

Figure 14. Pressure contours ([5]-Min).

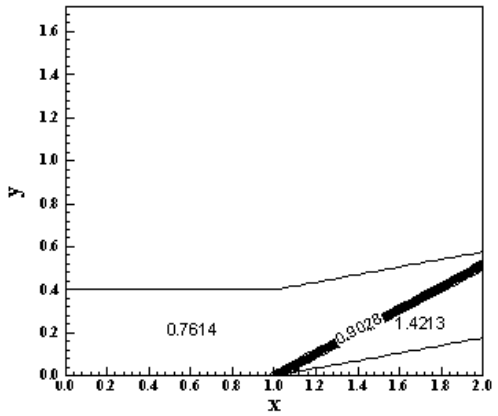

Figure 15. Pressure contours ([5]-Min).

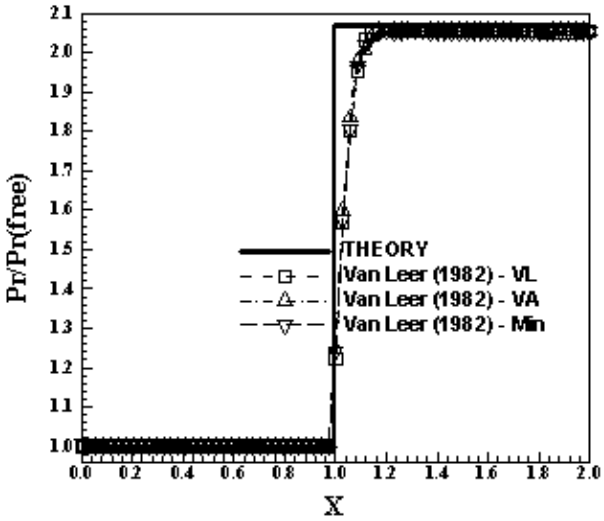

Figure 16. Wall pressure distributions ([5]).

Using a transfer in Figures 11, 13 and 15, it is possible to obtain the values of the shock angle of the oblique shock wave, β, to each variant of the [5] TVD scheme, as well the respective errors, shown in Tab. 2. As can be observed, the best variant was the [5] TVD scheme using VA limiter, with a percentage error of 0.00%.

Table 2. Shock angle of the oblique shock wave at the compression corner and percentage error ([5]).

Scheme	β (°)	Error (%)
[5]-VL	27.8	1.09
[5]-VA	27.5	0.00
[5]-Min	27.6	0.36

Figures 17 to 22 exhibit the pressure contours obtained by the scheme of [6] in its three variants: VL, VA and Min. Figures 17 and 18 show the pressure contours obtained by the [6] TVD scheme, using the VL limiter, in three-dimensions and at the xy plane, respectively. Figures 19 and 20 present the pressure contours obtained by the [6] TVD scheme, using VA limiter, in three-dimensions and at the xy plane, respectively. Finally, Figures 21 and 22 exhibit the pressure contours obtained by the [6] TVD scheme, using Min limiter, in three-dimensions and at the xy plane, respectively. As can be observed, the most intense pressure field was obtained by the [6] TVD scheme using VA limiter.

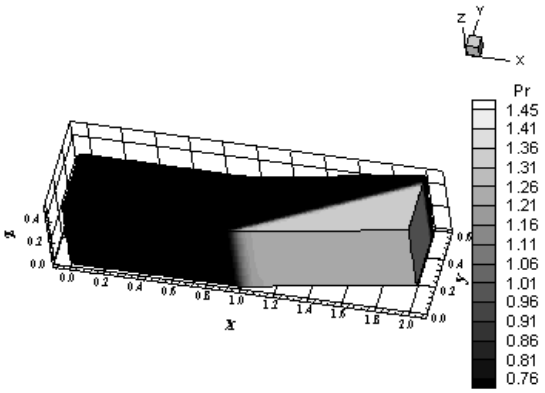

Figure 17. Pressure contours ([6]-VL).

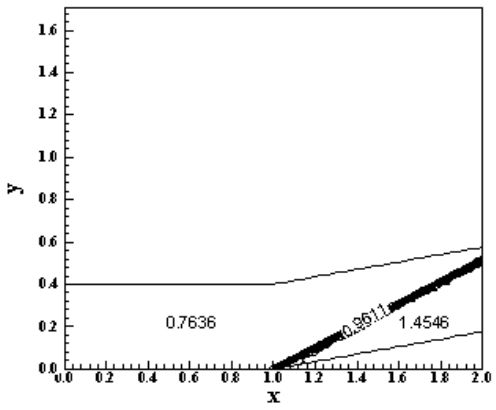

Figure 18. Pressure contours ([6]-VL).

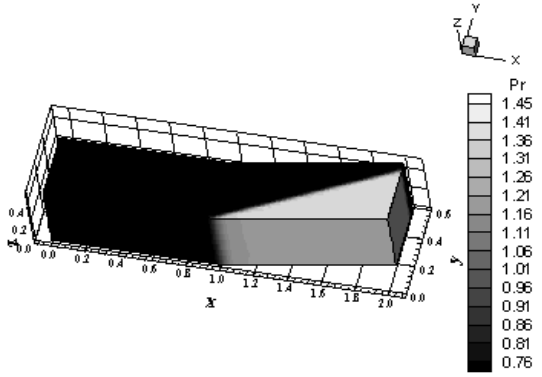

Figure 19. Pressure contours (LS-VA).

Figure 23 shows the wall pressure distributions obtained by the three variants of the [6] TVD scheme. They are compared with the oblique shock wave theory. As can be observed, all solutions present good pressure distributions, capturing the shock discontinuity in four cells, which is a reasonable result in terms of high resolution schemes. The best wall pressure distribution involving the [6] TVD variants is due to the Min limiter.

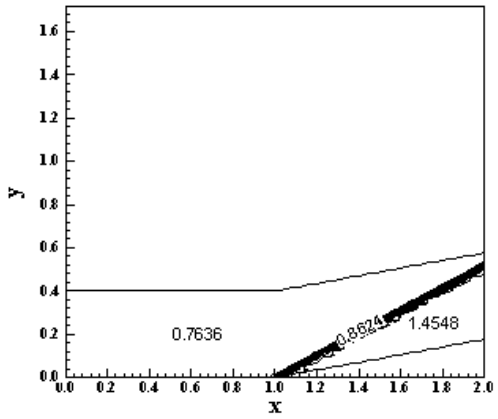

Figure 20. Pressure contours ([6]-VA).

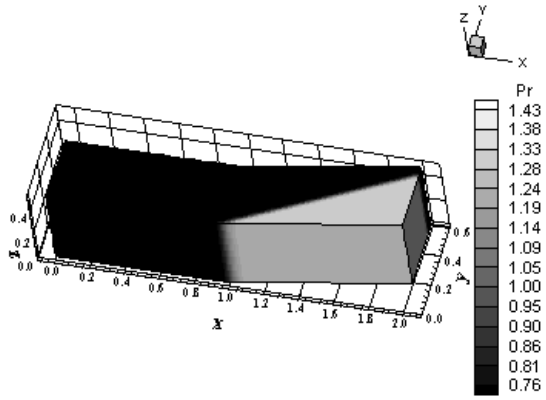

Figure 21. Pressure contours ([6]-Min).

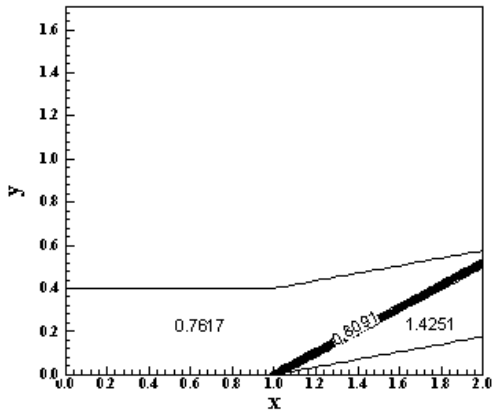

Figure 22. Pressure contours ([6]-Min).

Using a transfer in Figures 18, 20 and 22, it is possible to obtain the values of the shock angle of the oblique shock wave, β, to each variant of the [6] TVD scheme, as well the respective errors, shown in Tab. 3. As can be observed, the [6] TVD scheme using all three limiters yield the correct value, with a percentage error of 0.00%.

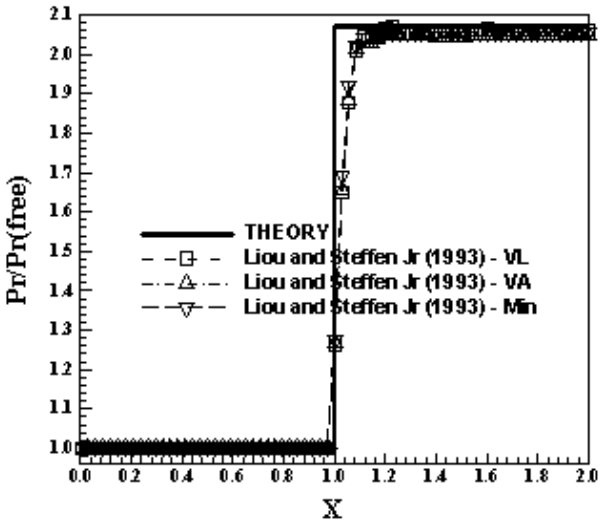

Figure 23. Wall pressure distributions ([6]).

Table 3. Shock angle of the oblique shock wave at the compression corner and percentage error ([6]).

Scheme	β (°)	Error (%)
[6]-VL	27.5	0.00
[6]-VA	27.5	0.00
[6]-Min	27.5	0.00

Figures 24 to 29 exhibit the pressure contours obtained by the scheme of [7] in its three variants: VL, VA and Min. Figures 24 and 25 show the pressure contours obtained by the [7] TVD scheme, using the VL limiter, in three-dimensions and at the xy plane, respectively. Figures 26 and 27 present the pressure contours obtained by the [7] TVD scheme, using VA limiter, in three-dimensions and at the xy plane, respectively. Finally, Figures 28 and 29 exhibit the pressure contours obtained by the [7] TVD scheme, using Min limiter, in three-dimensions and at the xy plane, respectively. As can be observed, the most intense pressure field was obtained by the [7] TVD scheme using VL limiter.

Figure 30 shows the wall pressure distributions obtained by the three variants of the [7] TVD scheme. They are compared with the oblique shock wave theory results. As can be observed, all solutions present good pressure distributions,

capturing the shock discontinuity in four cells, which is a reasonable result in terms of high resolution schemes. The best wall pressure distribution involving the [7] TVD variants is due to VA limiter.

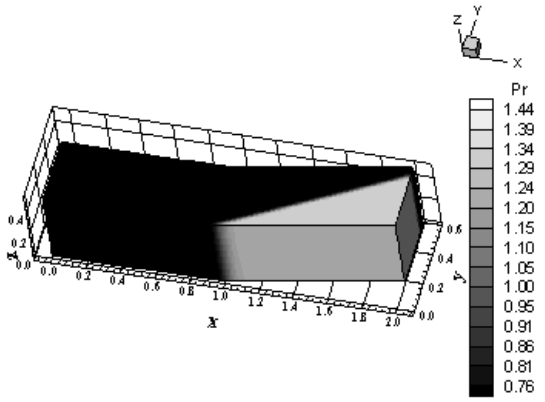

Figure 24. Pressure contours ([7]-VL).

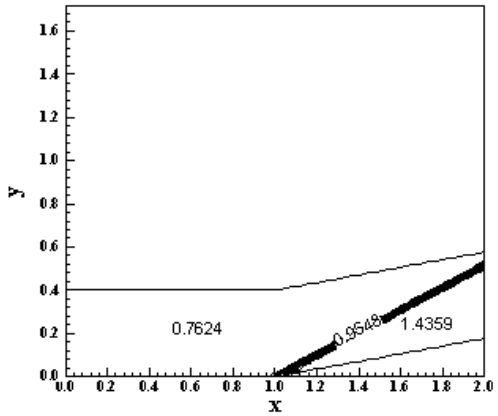

Figure 25. Pressure contours ([7]-VL).

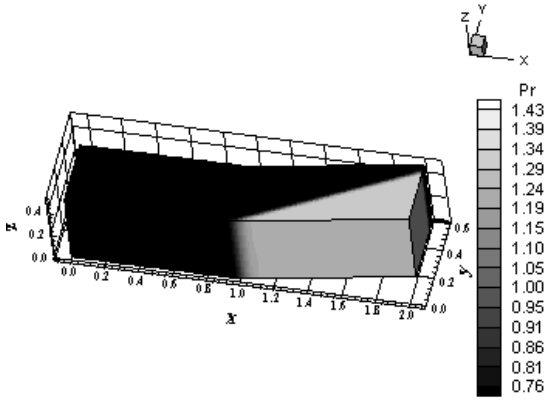

Figure 26. Pressure contours ([7]-VA).

Using a transfer in Figures 25, 27 and 29, it is possible to obtain the values of the shock angle of the oblique shock wave, β, to each variant of the [7] TVD scheme, as well the respective errors, shown in Tab. 4. As can be observed, the best variant was the [7] TVD scheme using Min limiter, with a percentage error of 0.00%.

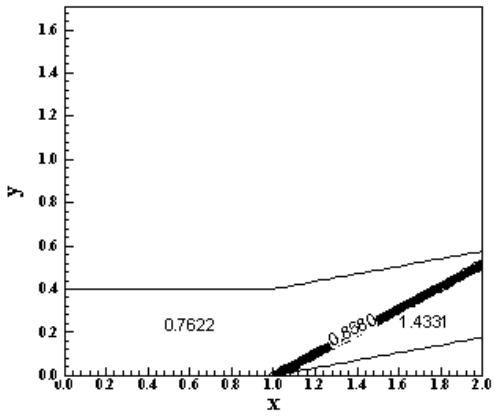

Figure 27. Pressure contours ([7]-VA).

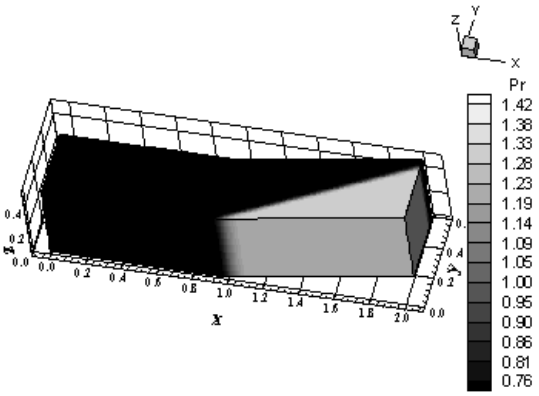

Figure 28. Pressure contours ([7]-Min).

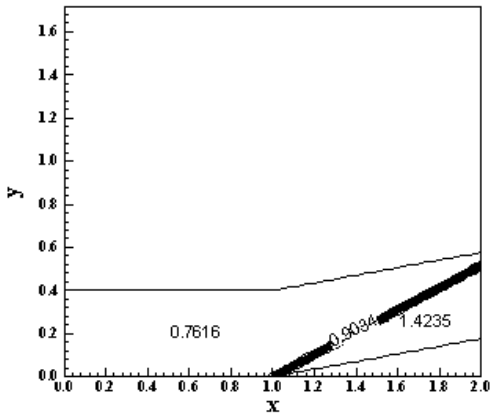

Figure 29. Pressure contours (RK-Min).

As global conclusion, the most severe pressure field was obtained by the [6] scheme using VA limiter. The best wall pressure distributions obtained by each scheme is shown in Fig. 31. The best wall pressure distribution among the distributions presented is due to [6] using Min limiter.

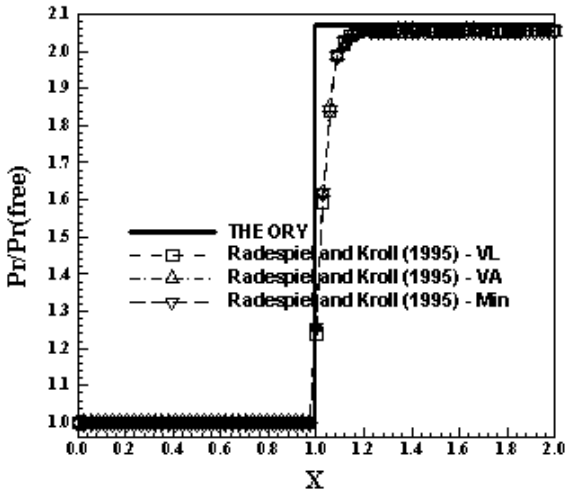

Figure 30. Wall pressure distributions ([7]).

Table 4. Shock angle of the oblique shock wave at the compression corner and percentage error ([7]).

Scheme	β (°)	Error (%)
[7]-VL	27.7	0.73
[7]-VA	27.8	1.09
[7]-Min	27.5	0.00

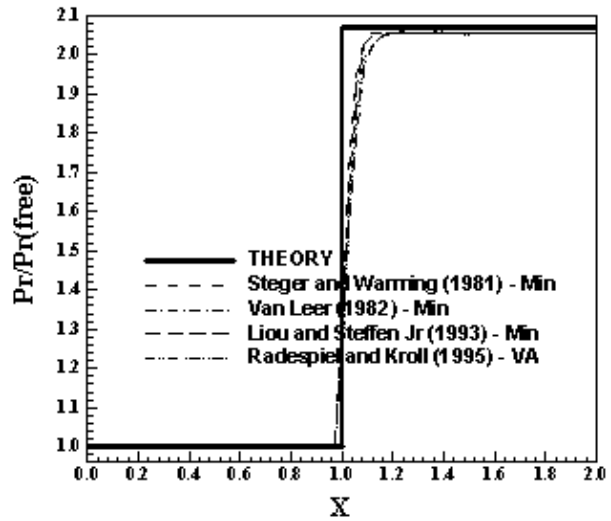

Figure 31. Best wall pressure distributions.

Table 5 presents the best values of the shock angle of the oblique shock wave obtained by each scheme. Except the [4] TVD scheme, all other schemes always present a variant with the correct value of the shock angle. As the [6] TVD scheme has presented the best wall pressure distribution using Min limiter and as it also presents the correct value of the shock angle of the oblique shock wave with this variant (the other two limiters too), the best scheme in this inviscid simulation is due to the [6] scheme using Min limiter.

Table 5. Best shock angles of the oblique shock wave at the compression corner and percentage error.

Scheme	β (°)	Error (%)
[4]-VL	27.6	0.36
[5]-VA	27.5	0.00
[6]-Min	27.5	0.00
[7]-Min	27.5	0.00

12.2 Viscous Results

The physical problem studied in the viscous laminar and turbulent simulations is the flow along a ramp. This problem is a supersonic flow hitting a ramp with 20° of inclination. It generates a shock and an expansion fan. The freestream Mach number adopted as initial condition to this simulation was 3.0, characterizing a moderate supersonic flow. The Reynolds number was estimated to be 2.419×10^5 at a flight altitude of 20,000m and l = 0.0437m, based on the work of [21]. To this Mach number and Reynolds number, a separated flow is formed at the ramp wall, with the formation of a circulation bubble. This behavior is observed in all solutions of all schemes.

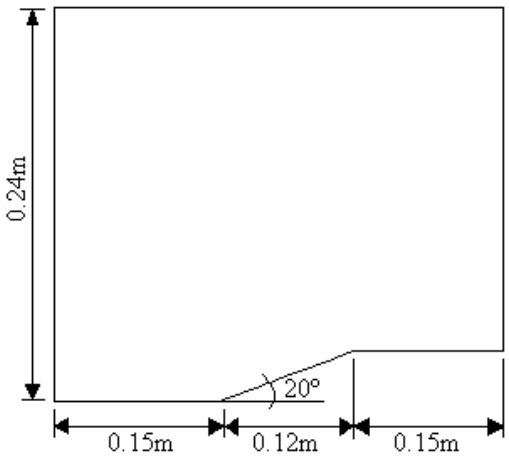

Figure 32. Ramp configuration in the xy plane.

The ramp configuration at the xy plane is described in Fig. 32. The compression corner has 20° of inclination. Its spanwise length is 0.25m. The mesh used in the simulations has 31,860 hexahedrons and 36,600 nodes to a structured discretization of the calculation domain. This mesh is equivalent, in finite differences, of being

composed of 61 points in the ξ direction, 60 points in the η direction and 10 points in the ζ direction. An exponential stretching of 10% in the η direction was employed. Figure 33 shows such mesh.

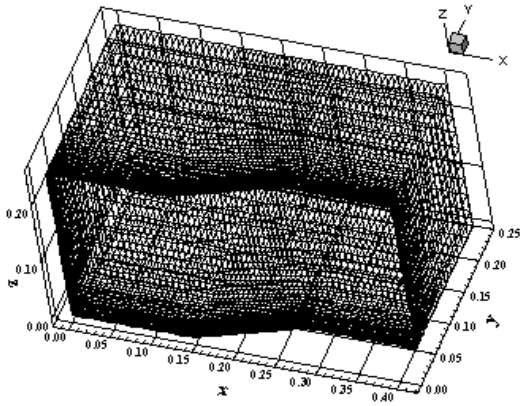

Figure 33. Ramp mesh in three-dimensions.

12.2.1 Laminar Case

Figures 34 to 39 exhibit the pressure contours and the streamlines of the velocity vector field generated by the [4] TVD scheme in its three variants, namely: VL, VA and Min. Figures 34 and 35 show the pressure contours and the streamlines, respectively, obtained by the [4] TVD scheme using VL limiter; Figures 36 and 37 show the pressure contours and the streamlines, respectively, obtained by the [4] TVD scheme using VA limiter; and Figures 38 and 39 show the pressure contours and the streamlines, respectively, obtained by the [4] TVD scheme using Min limiter. All solutions highlight the circulation bubble that is formed close to the ramp wall. The [4] TVD scheme using VA limiter yields the most severe pressure field, which characterizes the most conservative solution, involving the variants of this scheme. Good symmetry and homogeneity properties at the k planes are observed in all solutions. The shock wave is well captured. The circulation bubble is also well captured by all three limiters.

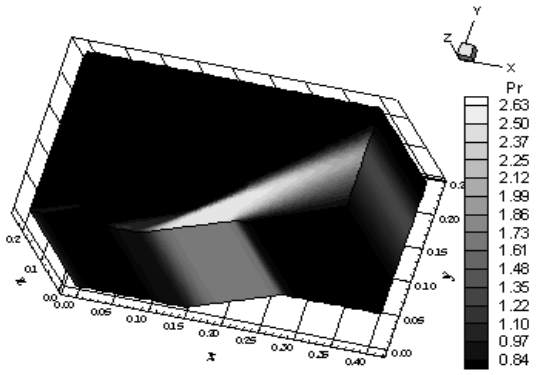

Figure 34. Pressure contours ([4]-VL).

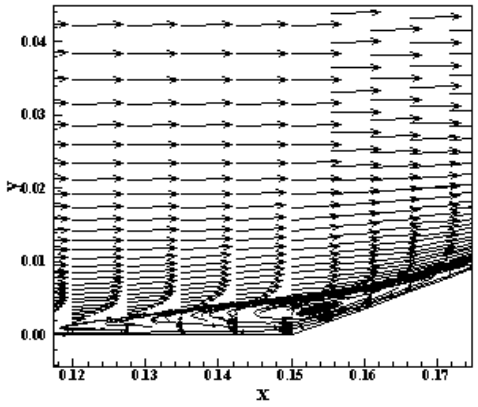

Figure 35. Streamlines and circulation bubble ([4]-VL).

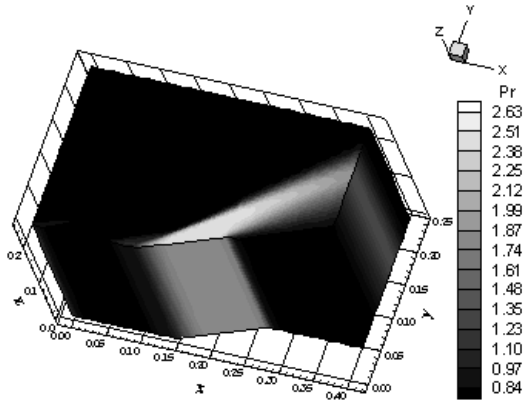

Figure 36. Pressure contours ([4]-VA).

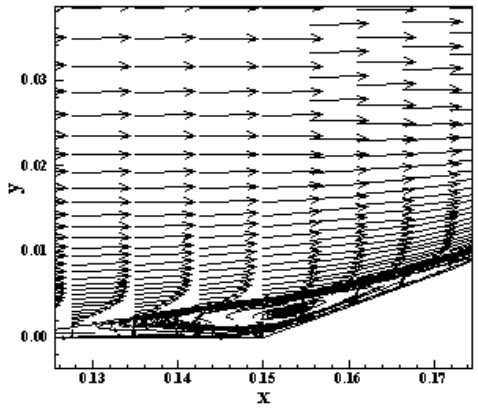

Figure 37. Streamlines and circulation bubble ([4]-VA).

Figure 40 exhibits the wall pressure distribution obtained by the three variants of the [4] TVD scheme. They are compared with the oblique shock wave and the expansion wave Prandtl-Meyer theory results, which are the correct solutions, according to the boundary layer theory (normal pressure gradient to the wall equal to zero). All schemes detect ahead of the ramp beginning a weaker shock, which is formed due to the increase of the boundary layer thickness in this region, because of the flow

separation, and the formation of the circulation bubble. This weaker shock is represented by an increase in the pressure ratio before the ramp. All three variants of the [4] TVD scheme capture the shock plateau appropriately, according to the inviscid solution, which represents a good signal of accuracy. The pressure recovery at the end of the expansion fan is well detected by all three variants of the [4] TVD scheme.

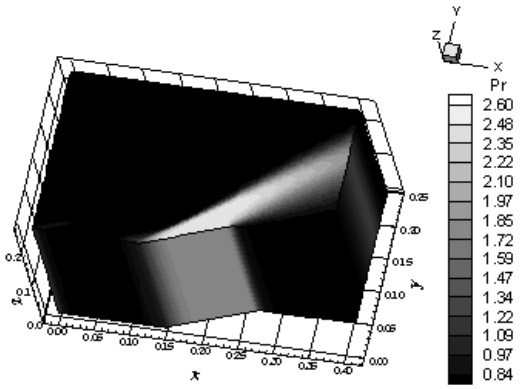

Figure 38. Pressure contours ([4]-Min).

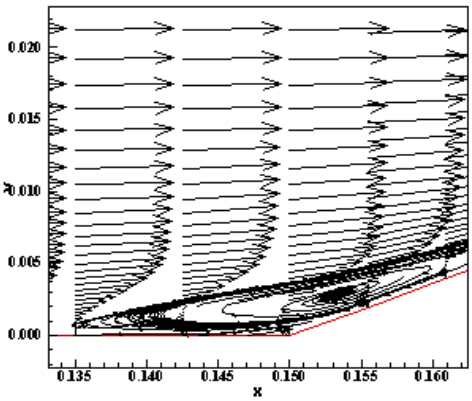

Figure 39. Streamlines and circulation bubble ([4]-Min).

Table 6 shows the detachment and reattachment points obtained by the three limiters studied with the [4] TVD scheme. The region of flow separation with minimum extent is due to [4] TVD scheme using Min limiter and with the maximum extent is due to [4] TVD scheme using VL limiter.

Again, one way to quantitatively verify if the solutions generated by each scheme are satisfactory consists in determining the shock angle of the oblique shock wave, β, measured in relation to the initial direction of the flow field. To the ramp problem, $\phi = 20^{o}$ (ramp inclination angle) and the freestream Mach number is 3.0, resulting from this diagram a value to β equal to 37.7º. Using a transfer in Figures 34, 36 and 38, considering the xy plane, it is possible to obtain the values of β to each scheme, as well the respective errors, shown in Tab. 7. As can be observed, the best scheme was the [4] TVD one using Min limiter, with an error of 0.53% (less than 1.0%).

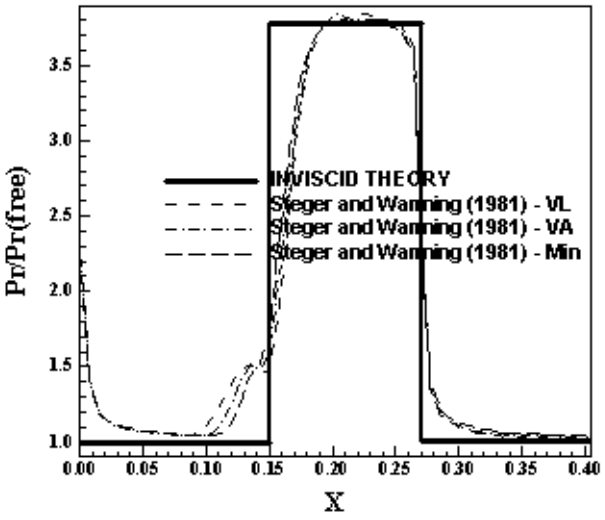

Figure 40. Wall pressure distributions ([4]-Lam).

Table 6. Flow separation detachment and reattachment points ([4]-Laminar).

Scheme	Detachment (m)	Reattachment (m)
[4]-VL	0.1125	0.1720
[4]-VA	0.1200	0.1664
[4]-Min	0.1350	0.1665

Table 7. Shock angle of the oblique shock wave at the ramp and percentage error ([4]-Laminar).

Scheme	β (°)	Error (%)
[4]-VL	37.0	1.86
[4]-VA	37.0	1.86
[4]-Min	37.5	0.53

As conclusion of the study analyzing the [4] TVD scheme in its three variants, the best variant is the [4] TVD scheme using Min limiter due to better accuracy than the others limiters in the determination of the shock angle and a minimum extent of the separation region, which agrees favorably with the turbulent results (to see in the next paper of this series).

Figures 41 to 44 exhibit the pressure contours and the streamlines of the velocity vector field generated by the [5] TVD scheme in its two variants, namely: VA and Min. The VL limiter did not produce converged results. Figures 41 and 42

show the pressure contours and the streamlines, respectively, obtained by the [5] TVD scheme using VA limiter;

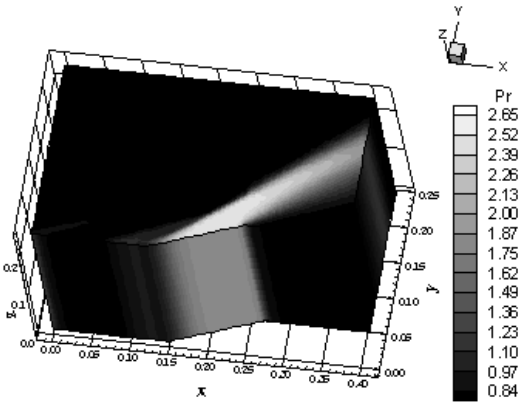

Figure 41. Pressure contours ([5]-VA).

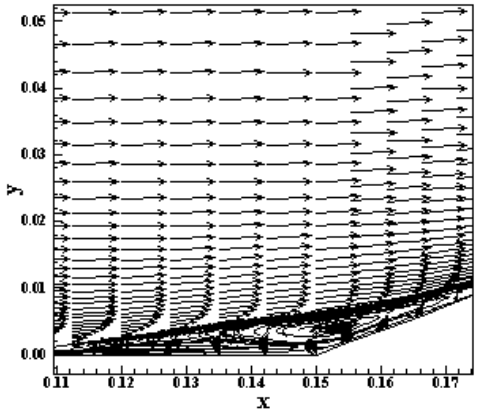

Figure 42. Streamlines and circulation bubble ([5]-VA).

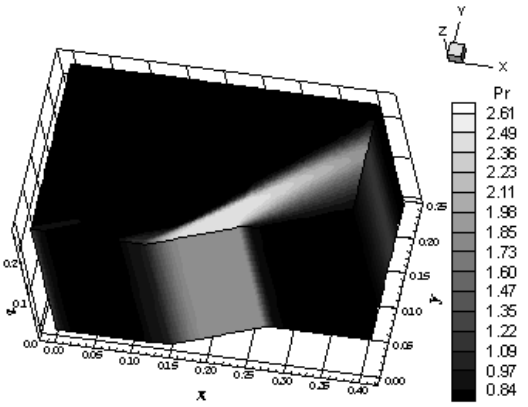

Figure 43. Pressure contours ([5]-Min).

and Figures 43 and 44 show the pressure contours and the streamlines, respectively, obtained by the [5] TVD scheme using Min limiter. The [5] TVD scheme using VA limiter yields the most severe pressure field, which characterizes the most conservative solution, involving the variants of this scheme. Good symmetry and homogeneity properties at the k planes are observed in all solutions. The shock wave is well captured. The circulation bubble is also well captured by the two limiters.

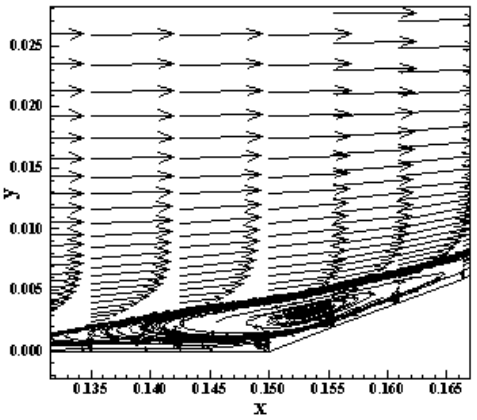

Figure 44. Streamlines and circulation bubble ([5]-Min).

Figure 45 exhibits the wall pressure distribution obtained by the two variants of the [5] TVD scheme. They are compared with the oblique shock wave and the expansion wave Prandtl-Meyer theory results, which are the correct solutions, according to the boundary layer theory. All schemes detect ahead of the ramp beginning a weaker shock. This weaker shock is represented by an increase in the pressure ratio ahead of the ramp.

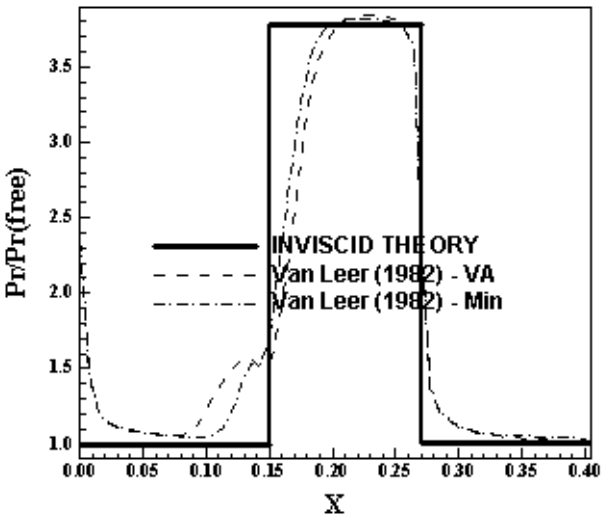

Figure 45. Wall pressure distributions ([5]-Lam).

Both variants of the [5] TVD scheme capture the shock plateau appropriately, according to the inviscid solution, which represents a good signal of accuracy. The pressure recovery at the end of the

expansion fan is well detected by both variants of the [5] TVD scheme.

Table 8 shows the detachment and reattachment points obtained by the two limiters studied with the [5] TVD scheme. The region of flow separation with minimum extent is due to [5] TVD scheme using Min limiter.

Table 8. Flow separation detachment and reattachment points ([5]-Laminar).

Scheme	Detachment (m)	Reattachment (m)
[5]-VA	0.1050	0.1830
[5]-Min	0.1275	0.1720

Using a transfer in Figures 41 and 43, considering the xy plane, it is possible to obtain the values of the shock angle of the oblique shock wave, β, to each variant of the [5] TVD scheme, as well the respective errors, shown in Tab. 9. As can be observed, the best variant was the [5] TVD scheme using Min limiter, with a percentage error of 0.53%.

Table 9. Shock angle of the oblique shock wave at the ramp and percentage error ([5]-Laminar).

Scheme	β (°)	Error (%)
[5]-VA	37.0	1.86
[5]-Min	37.9	0.53

As conclusion of the study analyzing the [5] TVD scheme in its two variants, the best variant is the [5] scheme using Min limiter due to better accuracy than the VA limiter in the determination of the shock angle and a minimum extent of the separation region, which agrees favorably with the turbulent results (to see in the next paper of this series).

Figures 46 to 51 exhibit the pressure contours and the streamlines of the velocity vector field generated by the [6] TVD scheme in its three variants, namely: VL, VA and Min. Figures 46 and 47 show the pressure contours and the streamlines, respectively, obtained by the [6] TVD scheme using VL limiter; Figures 48 and 49 show the pressure contours and the streamlines, respectively, obtained by the [6] TVD scheme using VA limiter; and Figures 50 and 51 show the pressure contours and the streamlines, respectively, obtained by the [6] TVD scheme using Min limiter. The [6] TVD scheme using VA limiter yields the most severe pressure field, which characterizes the most conservative solution, involving the variants of this scheme. Good symmetry and homogeneity properties at the k planes are observed in all solutions. The shock wave is well captured. The circulation bubble is also well captured by the three limiters.

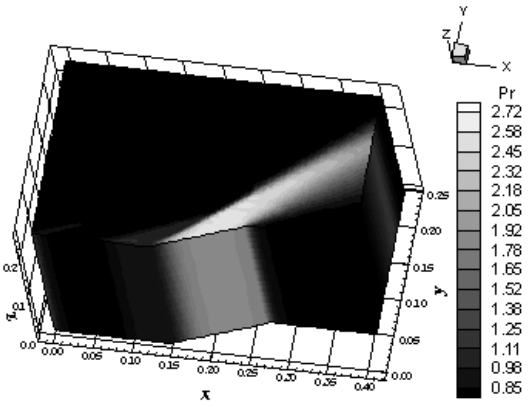

Figure 46. Pressure contours ([6]-VL).

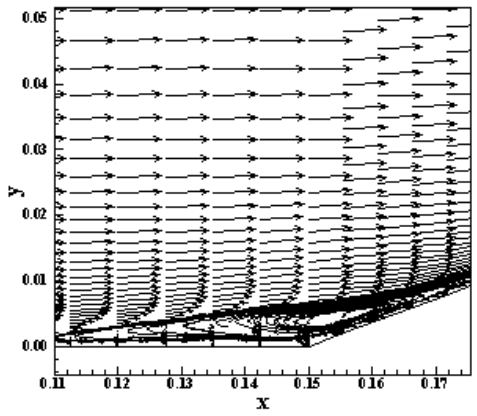

Figure 47. Streamlines and circulation bubble ([6]-VL).

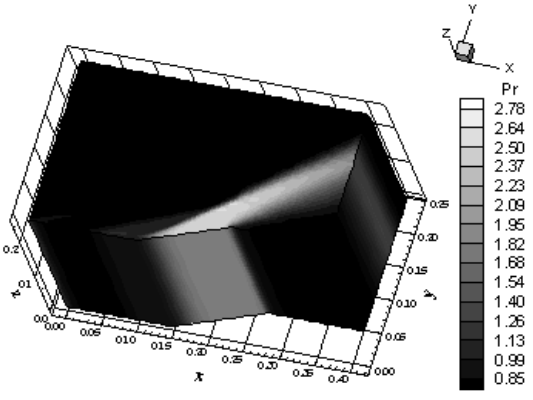

Figure 48. Pressure contours ([6]-VA).

Figure 52 exhibits the wall pressure distribution obtained by all three variants of the [6] TVD scheme. They are compared with the oblique shock wave and the expansion wave Prandtl-Meyer theory results.

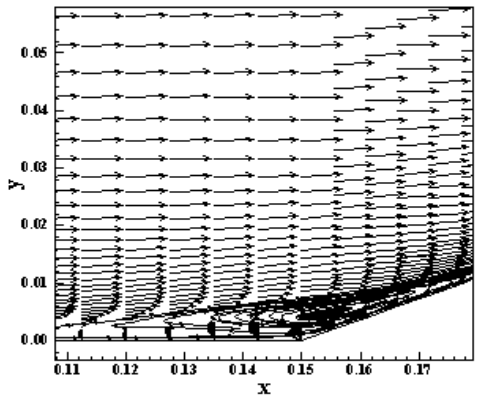

Figure 49. Streamlines and circulation bubble ([6]-VA).

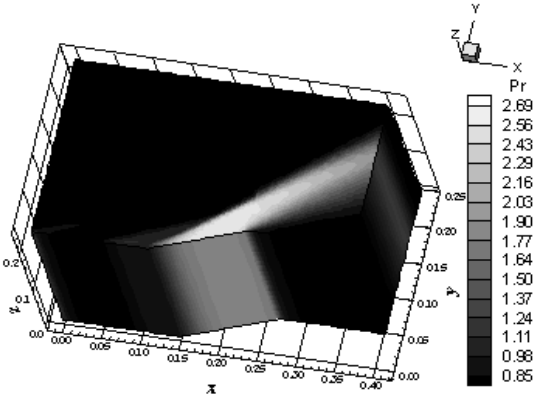

Figure 50. Pressure contours ([6]-Min).

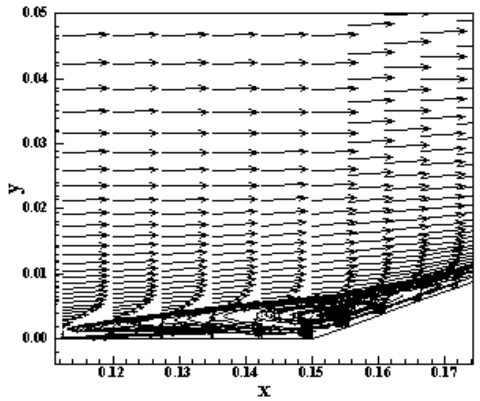

Figure 51. Streamlines and circulation bubble ([6]-Min).

All schemes detect ahead of the ramp beginning a weaker shock, which is formed due to the increase of the boundary layer thickness in this region, because of the flow separation, and the formation of the circulation bubble. All three variants of the [6] TVD scheme slightly over-predict the shock plateau, presenting a small divergence in relation to the inviscid solution. The pressure recovery at the end of the expansion fan is well detected by all three variants of the [6] TVD scheme.

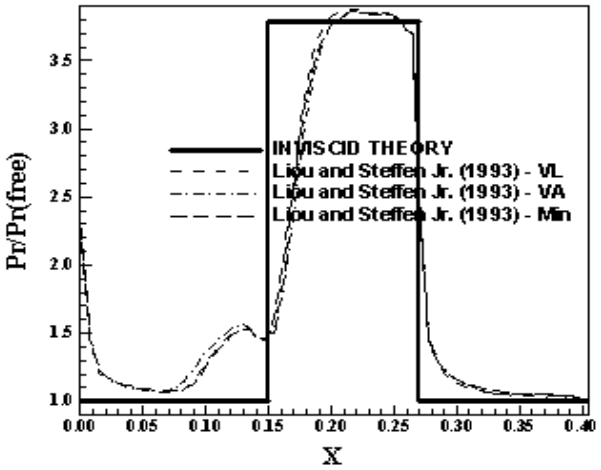

Figure 52. Wall pressure distributions ([6]-Lam).

Table 10 shows the detachment and reattachment points obtained by the three limiters studied with the [6] TVD scheme. The region of flow separation with minimum extent is due to [6] TVD scheme using VL and Min limiter.

Table 10. Flow separation detachment and reattachment points ([6]-Laminar).

Scheme	Detachment (m)	Reattachment (m)
[6]-VL	0.1050	0.1827
[6]-VA	0.0975	0.1882
[6]-Min	0.1050	0.1827

Using a transfer in Figures 46, 48 and 50, considering the xy plane, it is possible to obtain the values of the shock angle of the oblique shock wave, β, to each variant of the [6] TVD scheme, as well the respective errors, shown in Tab. 11. As can be observed, the best variant was the [6] TVD scheme using Min limiter, with a percentage error of 0.53%.

Table 11. Shock angle of the oblique shock wave at the ramp and percentage error ([6]-Laminar).

Scheme	β (°)	Error (%)
[6]-VL	38.5	2.12
[6]-VA	37.2	1.33
[6]-Min	37.9	0.53

As conclusion of the study analyzing the [6] TVD scheme in its three variants, the best variant is the [6] TVD scheme using Min limiter due to better accuracy than the other limiters in the determination of the shock angle and a minimum extent of the

separation region, which agrees favorably with the turbulent results (to see in the next paper of this series).

Figures 53 to 58 exhibit the pressure contours and the streamlines of the velocity vector field generated by the [7] TVD scheme in its three variants, namely: VL, VA and Min. Figures 53 and 54 show the pressure contours and the streamlines, respectively, obtained by the [7] TVD scheme using VL limiter; Figures 55 and 56 show the pressure contours and the streamlines, respectively, obtained by the [7] TVD scheme using VA limiter; and Figures 57 and 58 show the pressure contours and the streamlines, respectively, obtained by the [7] TVD scheme using Min limiter. All solutions highlight the circulation bubble formed at the ramp wall.

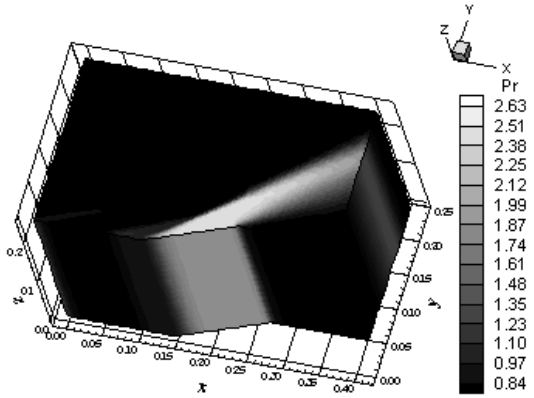

Figure 53. Pressure contours ([7]-VL).

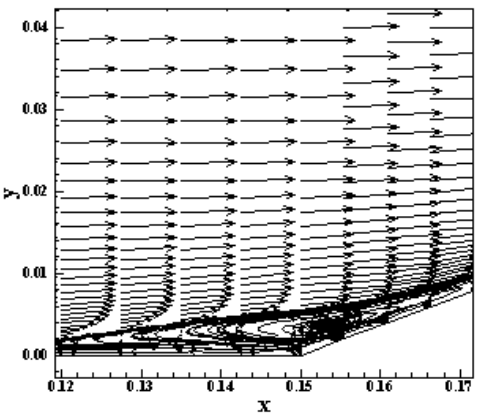

Figure 54. Streamlines and circulation bubble ([7]-VL).

The [7] TVD scheme using VA limiter yields the most severe pressure field, which characterizes the most conservative solution, involving the variants of this scheme. Good symmetry and homogeneity properties at the k planes are observed in all solutions. The shock wave is well captured. The circulation bubble is also well captured by the three limiters.

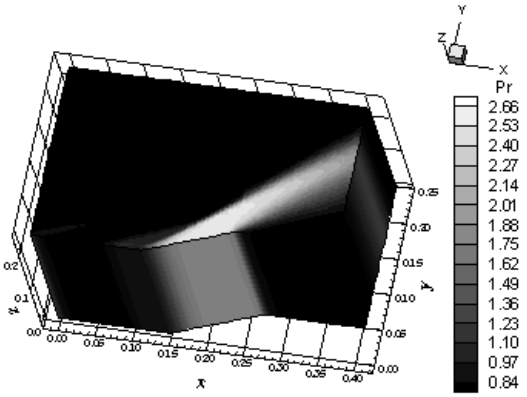

Figure 55. Pressure contours ([7]-VA).

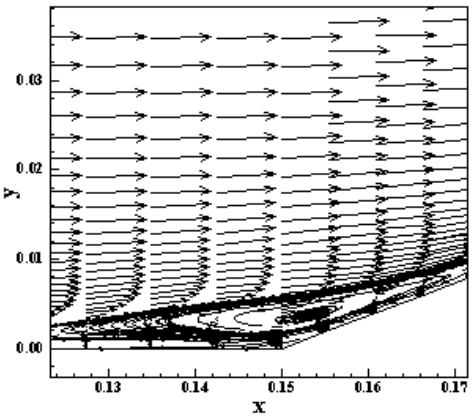

Figure 56. Streamlines and circulation bubble ([7]-VA).

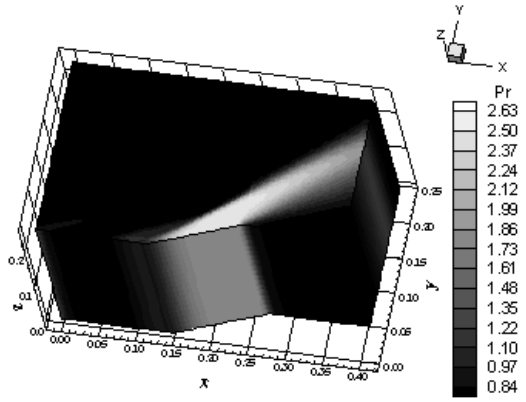

Figure 57. Pressure contours ([7]-Min).

Figure 59 exhibits the wall pressure distribution obtained by all three variants of the [7] TVD scheme. They are compared with the oblique shock wave and the expansion wave Prandtl-Meyer theory results. All schemes detect ahead of the ramp beginning a weaker shock. This weaker shock is represented by an increase in the pressure ratio

ahead of the ramp. All three variants of the [7] TVD scheme slightly over-predict the shock plateau, presenting a small divergence in relation to the inviscid solution. The pressure recovery at the end of the expansion fan is well detected by all three variants of the [7] TVD scheme.

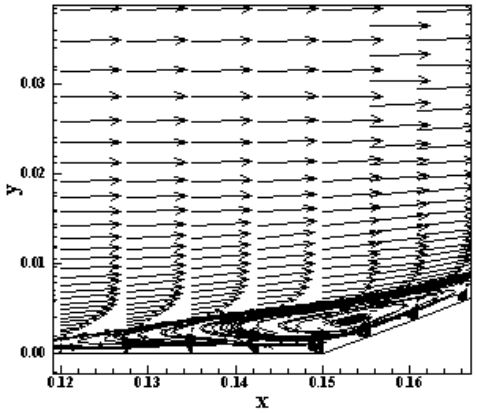

Figure 58. Streamlines and circulation bubble ([7]-Min).

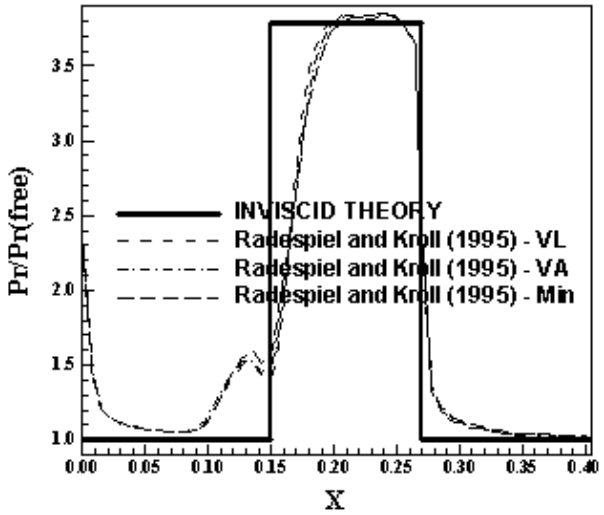

Figure 59. Wall pressure distributions ([7]-Lam).

Table 12 shows the detachment and reattachment points obtained by the three limiters studied with the [7] TVD scheme. All solutions present the same extent of the separated flow region.

Table 12. Flow separation detachment and reattachment points ([7]-Laminar).

Scheme	Detachment (m)	Reattachment (m)
[7]-VL	0.1125	0.1773
[7]-VA	0.1125	0.1773
[7]-Min	0.1125	0.1773

Using a transfer in Figures 53, 55 and 57, considering the xy plane, it is possible to obtain the values of the shock angle of the oblique shock wave, β, to each variant of the [7] TVD scheme, as well the respective errors, shown in Tab. 13. As can be observed, the best variant was the [7] TVD scheme using Min limiter, with a percentage error of 0.27%.

Table 13. Shock angle of the oblique shock wave at the ramp and percentage error ([7]-Laminar).

Scheme	β (°)	Error (%)
[7]-VL	37.9	0.53
[7]-VA	36.5	3.18
[7]-Min	37.6	0.27

As conclusion of the study analyzing the [7] TVD scheme in its three variants, the best variant is the [7] TVD scheme using Min limiter due to better accuracy than the others limiters in the determination of the shock angle.

As global conclusion, the most severe pressure field was obtained by the [6] scheme using VA limiter. The best wall pressure distributions are obtained by [4-5] TVD schemes in its variants. They present pressure plateau closer to the theoretical results than the [6-7] TVD schemes. The minimum extent of the separated flow region was detected by the [4] TVD scheme using Min limiter.

Table 14. Shock angle of the oblique shock wave at the ramp and percentage error (Best Results-Laminar).

Scheme	β (°)	Error (%)
[4]-Min	37.5	0.53
[5]-Min	37.9	0.53
[6]-Min	37.9	0.53
[7]-Min	37.6	0.27

Table 14 presents the best values of the shock angle of the oblique shock wave obtained by each scheme. The best result of all schemes, detecting more precisely the value of the shock angle, is due to [7] TVD scheme using Min limiter. As the [7] TVD scheme has presented the best value to the shock angle of the oblique shock wave with the Min variant, the best scheme in this viscous laminar simulation is due to the [7] scheme using Min limiter, although the [4] captures better pressure distribution and the minimum region of separated flow.

13 Conclusions

In the present work, the [4-7] schemes are implemented, on a finite volume context and using a structured spatial discretization, to solve the Euler and the laminar/turbulent Navier-Stokes equations in the three-dimensional space. All schemes are flux vector splitting ones and in their original implementations are first order accurate. A MUSCL approach is implemented in these schemes aiming to obtain second order spatial accuracy. The Van Leer, the Van Albada and the Minmod nonlinear limiters are employed to guarantee such accuracy and TVD high resolution properties. These flux vector splitting schemes employ approximate factorizations in ADI form to solve implicitly the Euler equations. To solve the laminar/turbulent Navier-Stokes equations, an explicit formulation based on a dimensional splitting procedure is employed. All schemes are first order accurate in time in their implicit and explicit versions. Turbulence is taken into account considering two algebraic models, namely: the [14-15] ones. The algorithms are accelerated to the steady state solution using a spatially variable time step, which has demonstrated effective gains in terms of convergence rate ([19-20]. All four schemes are applied to the solution of the physical problems of the supersonic flow along a compression corner, in the inviscid case, and of the supersonic flow along a ramp, in the laminar and turbulent cases. The results have demonstrated that the most severe and most accurate results are obtained with the [6] TVD high resolution scheme.

In the implicit inviscid case, the most severe pressure field was obtained by the [6] scheme using VA limiter. The best wall pressure distributions obtained by each scheme is shown in Fig. 31. The best wall pressure distribution among the distributions presented is due to [6] using Min limiter. Table 6 presents the best values of the shock angle of the oblique shock wave obtained by each scheme. Except the [4] TVD scheme, all other schemes always present a variant with the correct value of the shock angle. As the [6] TVD scheme has presented the best wall pressure distribution using Min limiter and as it also presents the correct value of the shock angle of the oblique shock wave with this variant (the other two limiters too), the best scheme in the inviscid simulation is due to the [6] scheme using Min limiter.

In the viscous case, the most severe pressure field was obtained by the [6] scheme using VA limiter. This behavior was observed in the laminar case and in the turbulent cases using the [14-15] models. The best wall pressure distributions are obtained by the [4] TVD scheme in its three variants, namely: VL, VA and Min, and by the [5] TVD scheme in its two variants, namely: VA and Min, in the laminar and in the turbulent case with the [15] model. These behaviors will be shown in the next paper of this series.

14 Acknowledgments

The present author acknowledges the CNPq by the financial support conceded under the form of a DTI (Industrial Technological Development) scholarship no. 384681/2011-5. He also acknowledges the infra-structure of the ITA that allowed the realization of this work.

References:

[1] P. Kutler, Computation of Three-Dimensional, Inviscid Supersonic Flows, *Lecture Notes in Physics*, Springer Verlag, Berlin, Vol. 41, 1975, pp. 287-374.

[2] J. L. Steger, Implicit Finite-Difference Simulation of Flow About Arbitrary Two-Dimensional Geometries, *AIAA Journal*, Vol. 16, No. 7, 1978, pp. 679-686.

[3] P. L. Roe, Approximate Riemann Solvers, Parameter Vectors, and Difference Schemes, *Journal of Computational Physics*, Vol. 43, 1981, 357-372.

[4] J. L. Steger, R. F. Warming, Flux Vector Splitting of the Inviscid Gasdynamic Equations with Application to Finite-Difference Methods, *Journal of Computational Physics*, Vol. 40, 1981, pp. 263-293.

[5] B. Van Leer, Flux-Vector Splitting for the Euler Equations, *Lecture Notes in Physics*, Vol. 170, 1982, pp. 507-512, Springer Verlag, Berlin.

[6] M. Liou, C. J. Steffen Jr., A New Flux Splitting Scheme, *Journal of Computational Physics*, Vol. 107, 1993, pp. 23-39.

[7] R. Radespiel, N. Kroll, Accurate Flux Vector Splitting for Shocks and Shear Layers, *Journal of Computational Physics*, Vol. 121, 1995, pp. 66-78.

[8] C. Hirsch, *Numerical Computation of Internal and External Flows – Computational Methods for Inviscid and Viscous Flows*, John Wiley & Sons Ltd, 691p, 1990.

[9] R. M. Beam, R. F. Warming, An Implicit Factored Scheme for the Compressible Navier-Stokes Equations, *AIAA Journal*, Vol. 16, No. 4, 1978, pp. 393-402.

[10] J. Douglas, On the Numerical Integration of $u_{xx}+u_{yy}=u_t$ by Implicit Methods, *Journal of*

the Society of Industrial and Applied Mathematics, Vol. 3, 1955, pp. 42-65

[11] D. W. Peaceman, H. H. Rachford, The Numerical Solution of Parabolic and Elliptic Differential Equations, *Journal of the Society of Industrial and Applied Mathematics*, Vol. 3, 1955, pp. 28-41.

[12] J. Douglas, J. E. Gunn, A General Formulation of Alternating Direction Methods, *Numerische Mathematiks*, Vol. 6, 1964, pp. 428-453.

[13] N. N. Yanenko, *The Method of Fractional Steps*, Springer Verlag, NY, EUA, 1971.

[14] T. Cebeci, A. M. O. and Smith, A Finite-Difference Method for Calculating Compressible Laminar and Turbulent Boundary Layers, *Journal of Basic Engineering*, Trans. ASME, Series B, Vol. 92, No. 3, 1970, pp. 523-535.

[15] B. D. Baldwin, H. Lomax, Thin Layer Approximation and Algebraic Model for Separated Turbulent Flows, *AIAA Paper 78-257*, 1978.

[16] E. S. G. Maciel, Turbulent Flow Simulations Using the MacCormack and the Jameson and Mavriplis Algorithms Coupled with the Cebeci and Smith and the Baldwin and Lomax Models in Three-Dimensions, *Engineering Applications of Computational Fluid Mechanics*, China, Vol. 1, No. 3, 2007, pp. 147-163.

[17] R. W. MacCormack, The Effect of Viscosity in Hypervelocity Impact Cratering, *AIAA Paper 69-354*, 1969.

[18] A. Jameson, D. J. Mavriplis, Finite Volume Solution of the Two-Dimensional Euler Equations on a Regular Triangular Mesh, *AIAA Journal* Vol. 24, No. 4, 1986, pp. 611-618, 1986.

[19] E. S. G. Maciel, Analysis of Convergence Acceleration Techniques Used in Unstructured Algorithms in the Solution of Aeronautical Problems – Part I, *Proceedings of the XVIII International Congress of Mechanical Engineering (XVIII COBEM)*, Ouro Preto, MG, Brazil, 2005. [CD-ROM]

[20] E. S. G. Maciel, Analysis of Convergence Acceleration Techniques Used in Unstructured Algorithms in the Solution of Aerospace Problems – Part II, *Proceedings of the XII Brazilian Congress of Thermal Engineering and Sciences (XII ENCIT)*, Belo Horizonte, MG, Brazil, 2008. [CD-ROM]

[21] R. W. Fox, A. T. McDonald, *Introdução à Mecânica dos Fluidos*, Ed. Guanabara Koogan, Rio de Janeiro, RJ, Brazil, 632p, 1988.

[22] E. S. G. Maciel, Comparação entre os Algoritmos de MacCormack e de Jameson e Mavriplis na Solução das Equações de Euler e de Navier-Stokes no Espaço Tridimensional, M*ecánica Computacional Journal*, Argentina, Vol. XXIV, No. 12, 2005, pp. 2055-2074.

[23] E. S. G. Maciel, Solutions of the Euler Equations Using Implicit TVD High Resolution Algorithms in Three-Dimensions, *Mecánica Computacional Journal*, Argentina, Vol. XXVIII, No. 18, 2009, pp. 1517-1541.

[24] L. N. Long, M. M. S. Khan, H. T. Sharp, H. T., Massively Parallel Three-Dimensional Euler / Navier-Stokes Method. *AIAA Journal*, Vol. 29, No. 5, 1991, pp. 657-666.

[25] B. Van Leer, Towards the Ultimate Conservative Difference Scheme. II. Monotonicity and Conservation Combined in a Second-Order Scheme, *Journal of Computational Physics*, Vol. 14, 1974, pp. 361-370.

[26] P. L. Roe, 1983, *In Proceedings of the AMS-SIAM Summer Seminar on Large-Scale Computation in Fluid Mechanics*, Edited by B. E. Engquist *et al*, *Lectures in Applied Mathematics*, Vol. 22, 1983, p. 163.

[27] E. S. G. Maciel, Simulação Numérica de Escoamentos Supersônicos e Hipersônicos Utilizando Técnicas de Dinâmica dos Fluidos Computacional, *Doctoral Thesis*, ITA, São José dos Campos, SP, Brazil, 258p, 2002.

[28] J. T. Batina, Implicit Upwind Solution Algorithms for Three-Dimensional Unstructured Meshes, *AIAA Journal*, Vol. 31, No. 5, 1993, pp. 801-805.

[29] J. D. Anderson Jr., *Fundamentals of Aerodynamics*, McGraw-Hill, Inc., EUA, 563p, 1984.